Chapter 4

Superconvergent Beam Element with Magnetostrictive Patches

4.1 Introduction

In the last chapter, a series of Finite Element (FE) formulation were performed and these were applied to solve some health monitoring problems involving different flaws such as material degradation, delamination, fiber breakages, matrix cracking etc. In most cases, substantial flaw sizes were considered to induce a voltage change in the sensing coil. However, if the flaw size is very small, then one would require signal with high frequency content. From FE point of view, such a signal will enormously increase the problem sizes due to the requirement that the element size be comparable to the wavelength, which are very small at high frequencies. This problem can be alleviated to a certain level by using, what is known as super-convergent FE formulation.

One of the fundamental problems encountered in FE formulation is choice of appropriate polynomials of the field variable. For example, for obtaining accurate responses for the field variable (transverse displacement) in elementary beam, one needs a cubic polynomial, and the formulated element using such polynomial is a C^1 continuous element as it has to satisfy both displacement and slope continuity. On the other hand, for the same beam, if shear deformation is considered, this slope is independently interpolated along with transverse displacement and both these field variables require only linear polynomials. In other words, the formulation is C^0 continuous. If such an element is used in this beam situation, where the shear strains are negligible, the element's response will be many orders smaller than the true response. This phenomenon is called the "Shear locking problem" and so far is dealt in many references [313, 314, 427, 325, 32, 123, 347]. Normally one under-integrates the energy terms associated with the shear stress/strain

[313] to remove the locking. Alternatively, one can use the superconvergent solution to the governing equation as interpolating function for element formulation. This completely removes locking and some of the constants of the interpolating functions become material/sectional properties dependent. In this approach, the static part of the governing equation is exactly solved and used as interpolating function for element formulation. Hence, the approach gives exact static stiffness for point loads. Some of the constants in the interpolating function, when evaluated in term of nodal displacements, become dependent on material/sectional properties of the beam.

4.1.1 Existing Literature

Such approaches were adopted to develop elements for Herman-Mindlin rod [139], first-order shear deformable composite beam [62], first- and higher-order shear deformable isotropic beam [181, 325] and beam with Poisson's contraction [64]. Chakraborty et al. [63] developed such an element for functionally graded beam based on first order shear theory. Mitra et al. [268] developed super convergent element of arbitrary cross-section for composite thin wall beam with open or closed contour. Superconvergent solution for bending of isotropic beam based on higher order shear deformable theory (HSDT) was reported by Eisenberger [114]. Similar solutions for the bending of thin and thick cross-ply laminated beams were presented by Khedir and Reddy [180, 181] using the state space concept. Murthy et al. [283] developed a refined higher order finite element for asymmetric composite beams.

In this chapter, the super-convergent FE approach is used to derive two different beam elements with embedded magnetostrictive patches, one for Euler-Bernoulli beam and the other for a shear deformable beam. As a result, in most cases, only a single element is adequate to capture the static behavior irrespective of boundary conditions and ply-stacking configuration. As seen in the previous works, the coefficients associated with the interpolating polynomial are expected to be dependent on the material properties and the ply-stacking sequence. Finally these super-convergent elements will be used for material property identification using an Artificial Neural Network (ANN) model, where a number of finite element simulation is essential with different values of material properties to generate a mapping relation between structural response and material properties. These finite element simulations can be performed using very few formulated super-convergent elements, which can simultaneously reduce the computational time. Again, here, the elements will be formulated for both uncoupled and coupled material models and their effects on the response will be brought out in most of the examples solved in this chapter.

This chapter is organized as follows. First the variational formulation is presented to obtain the governing differential equations of Euler-Bernoulli and first order shear deformable beam. Both coupled and uncoupled constitutive models are discussed. This is followed by a section on numerical experiments, where, static and free vibration results are presented. This section concludes with an example that demonstrates the utility of this element in material property identification of magnetostrictive material through both polynomial and artificial neural network identification. The findings in this chapter are summarized at the end.

4.2 Super-Convergent Finite Element Formulations.

In this section, developments of two different finite elements are outlined: one based on the elementary (Bernoulli-Euler) theory and the other based on First order Shear Deformation (Timoshenko) theory. For each of these elements, FE model based on coupled and uncoupled properties of constitutive model of the magnetostrictive material, are formulated.

4.2.1 FE Formulation for Euler-Bernoulli Beam.

The foremost requirement for formulating super convergent elements is to derive the governing differential equation of the system. We do this here using Hamilton's principle. The displacement and magnetic field variation for the element is assumed as:

$$\begin{aligned} U(x,y,t) &= u^\circ(x,t) - z w^\circ_{,x}(x,t), \\ V(x,y,t) &= 0, \\ W(x,y,t) &= w^\circ(x,t), \\ H_x(x,y,t) &= H_{xp}(x,t), \end{aligned} \tag{4.1}$$

where U, V, W are the mechanical displacements in the three coordinate directions, u° and w° are the mid plane displacements of the laminate. The H_x is the magnetic field in the x direction, while H_{xp} is the magnetic field in the p^{th} patches. To handle magneto-thermo-mechanical analysis, we include the thermal variation in the strain distribution and it is given by

$$\epsilon_{xx} = \frac{\partial U}{\partial x} = u^\circ_x - z w^\circ_{,xx} - \alpha(\Delta T), \tag{4.2}$$

where α is the coefficient of thermal expansion and (ΔT) is the temperature rise. The constitutive relation for the beam with magnetostrictive patches is given by

$$\sigma_{xx} = \bar{Q}_{11}\epsilon_{xx} - e_{11}H, \qquad B_{xx} = e_{11}\epsilon_{xx} + \mu^{\epsilon}H, \tag{4.3}$$

where σ_{xx} and ϵ_{xx}, are normal stresses and normal strains in the x direction. The B_{xx} is the magnetic flux density in the x direction. Also $\bar{Q}_{11}$ is the material constant for mechanical loads, while e_{11} and μ^{ϵ} are magnetostrictive stress coefficient and strain permeability of the magnetostrictive material, respectively. In above expression, $H = H_{xp}$ is the magnetic field, which is basically the unknown for coupled constitutive model, and is equal to $H = nI$ for the uncoupled constitutive model, where I is coil current and n is the coil turn per unit length.

The strain energy (S), the energy due to magnetic field (W_m) and kinetic energy (T) are then given by

$$S = \frac{1}{2}\int_0^L \int_A (\sigma_{xx}\varepsilon_{xx})\, dA\, dx\ , \tag{4.4}$$

$$W_m = \int_0^L \int_A (\frac{1}{2}B_{xx}H + In\mu^{\sigma}H)\, dA\, dx\ , \tag{4.5}$$

$$T = \frac{1}{2}\int_0^L \int_A \varrho(z)(\dot{U}^2 + \dot{W}^2)\, dA\, dx\ , \tag{4.6}$$

where μ^{σ} is the permeability measured at constant stress. Here $(\dot{\ })$ denotes the time derivative; $\varrho(z)$, L and A are the density, the length and the area of cross-section of the beam, respectively. Applying Hamilton's principle, we get the following three governing equations corresponding to 3 degrees of freedom:

$$\begin{aligned}
\delta u^{\circ} :&\qquad I_0\ddot{u}^{\circ} - I_1\ddot{w}^{\circ}_{,x} + A_{11}u^{\circ}_{,xx} - B_{11}w^{\circ}_{,xxx} - \sum_p A^{e}_{11p}H_{xp,x} = 0,\\
\delta w^{\circ} :&\qquad I_0\ddot{w}^{\circ} + B_{11}u^{\circ}_{,xxx} - D_{11}w^{\circ}_{,xxxx} - \sum_p B^{e}_{11p}H_{xp,xx} = 0,\\
\delta H_{xp} :&\qquad A^{e}_{11p}u^{\circ}_{,x} - B^{e}_{11p}w^{\circ}_{,xx} + A^{\epsilon}_{\mu p}H_{xp} - In_pA^{\sigma}_{\mu p} - A^{e\alpha}_{11p}(\Delta T) = 0.
\end{aligned} \tag{4.7}$$

The associated three force boundary conditions are

$$\begin{aligned}
N &= -A_{11}u^{\circ}_{,x} + B_{11}w^{\circ}_{,xx} + \sum_p A^{e}_{11p}H_{xp} + A^{\alpha}_{11}\Delta T,\\
M &= B_{11}u^{\circ}_{,x} - D_{11}w^{\circ}_{,xx} - \sum_p B^{e}_{11}H_{xp} - B^{\alpha}_{11}\Delta T,\\
V &= -B_{11}u^{\circ}_{,xx} + D_{11}w^{\circ}_{,xxx} + \sum_p B^{e}_{11p}H_{xp,x},
\end{aligned} \tag{4.8}$$

where N is the axial force, M is the moment and V is the shear force. The cross sectional properties A_{ij}, B_{ij}, D_{ij}, A^e_{ijp}, B^e_{ijp}, I_0, I_1, I_2, $A^\epsilon_{\mu p}$ and $A^\sigma_{\mu p}$ are given by

$$[A_{ij} \quad B_{ij} \quad D_{ij}] = \int_A \bar{Q}_{ij}[1 \quad z \quad z^2]dA, \tag{4.9}$$

$$[A^e_{ijp} \quad B^e_{ijp}] = \int_p e_{ij}[1 \quad z]dA, \tag{4.10}$$

$$[I_0 \quad I_1 \quad I_2] = \int_A \rho[1 \quad z \quad z^2]dA, \tag{4.11}$$

$$[A^\epsilon_{\mu p} \quad A^\sigma_{\mu p}] = \int_p [\mu^\epsilon \quad \mu^\sigma]dA. \tag{4.12}$$

In the above expression, the integration over p means that this operation is performed only to p^{th} magnetostrictive layer. The cross-sectional thermal stiffness is given by

$$\left[A^\alpha_{ij} \quad B^\alpha_{ij}\right] = \int \alpha\bar{Q}_{ij}\left[1 \quad z\right]dA. \tag{4.13}$$

4.2.1.1 Uncoupled Formulation

For finite element beam formulation based on uncoupled constitutive model, we have $H_{xp} = H = nI, \partial H_{xp}/\partial x = 0$. Hence, the governing equations and the associated boundary conditions become

$$\begin{aligned} \delta u^\circ : &\qquad I_0\ddot{u}^\circ - I_1\ddot{w}^\circ_{,x} + A_{11}u^\circ_{,xx} - B_{11}w^\circ_{,xxx} = 0, \\ \delta w^\circ : &\qquad I_0\ddot{w}^\circ + B_{11}u^\circ_{,xxx} - D_{11}w^\circ_{,xxxx} = 0, \end{aligned} \tag{4.14}$$

and

$$\begin{aligned} N &= -A_{11}u^\circ_{,x} + B_{11}w^\circ_{,xx} + \sum_p A^e_{11p}H_{xp} + A^\alpha_{11}\Delta T, \\ M &= B_{11}u^\circ_{,x} - D_{11}w^\circ_{,xx} - \sum_p B^e_{11}H_{xp} - B^\alpha_{11}\Delta T, \\ V &= -B_{11}u^\circ_{,xx} + D_{11}w^\circ_{,xxx}. \end{aligned} \tag{4.15}$$

It is to be noted that the magnetic field will appear only in the force boundary conditions. The FE equation begins by solving Equation (4.14) exactly. Taking only the static parts of the Equation-(4.14) and simplifying, we can write it as

$$u^\circ_{,xxx} = 0, \qquad w^\circ_{,xxxx} = 0. \tag{4.16}$$

The solutions of Equation-(4.16), are:

$$u^\circ = c_0 + c_1 x + c_2 x^2, \quad w^\circ = c_3 + c_4 x + c_5 x^2 + c_6 x^3, \tag{4.17}$$

where $c_0, c_1, c_2, c_3, c_4, c_5, c_6$ are seven unknown constants to be determined from six nodal degrees of freedom ($u^\circ, w^\circ, \phi = \partial w^\circ/\partial x$ at the two nodes). Thus, there must be one dependent constant, which can be obtained by substituting Equation-(4.17) in Equation-(4.14) and Equation-(4.15). Introducing a variable β_e as

$$\beta_e = 3\frac{B_{11}}{A_{11}},$$

and substituting u° and w° in the static part of the governing differential equations (Equation-(4.14)), we get $c_2 = \beta_e c_6$. Hence, the modified displacement fields can now be written as

$$u^\circ = c_0 + c_1 x + \beta_e c_6 x^2, \qquad w^\circ = c_3 + c_4 x + c_5 x^2 + c_6 x^3. \tag{4.18}$$

For symmetric ply lay up, $B_{ij} = 0$ and hence $\beta_e = 0$. In this case axial and transverse deformation gets uncoupled and the interpolation function reduces to that of simple rod and Euler-Bernoulli beam, respectively. Equation-(4.18) can now be written in matrix notation as

$$\{u^\circ \quad w^\circ \quad w^\circ_{,x}\}^T = [N(x)]\{C\}, \tag{4.19}$$

where $[N(x)]$ is a matrix of dimension $3X6$, which contains functions of x, i.e., x, x^2 and x^3. The unknown constant vector $\{C\}$ is given by

$$\{C\} \quad = \quad \{c_0 \quad c_1 \quad c_3 \quad c_4 \quad c_5 \quad c_6\}^T. \tag{4.20}$$

First we relate the nodal degrees of freedom to the unknown constants by the definitions:

$$\begin{aligned} u^\circ(x=0) = u^\circ_1, \quad w^\circ(x=0) = w^\circ_1, \quad \phi^\circ(x=0) = \phi^\circ_1, \\ u^\circ(x=L) = u^\circ_2, \quad w^\circ(x=L) = w^\circ_2, \quad \phi^\circ(x=L) = \phi^\circ_2, \end{aligned} \tag{4.21}$$

which can be written in matrix notation as

$$\{u^e\} = \{u^\circ_1 \quad w^\circ_1 \quad \phi^\circ_1 \quad u^\circ_2 \quad w^\circ_2 \quad \phi^\circ_2\}^T = [G^{-1}]\{C\}, \tag{4.22}$$

and inverting this, we get

$$\{C\} = [G]\{u^e\}. \tag{4.23}$$

Now this vector $\{C\}$ is substituted in the Equation-(4.19) to get the mechanical displacement for any arbitrary location in terms of nodal displacements $\{u^e\}$ as

$$\{u^\circ \quad w^\circ \quad w^\circ_{,x}\}^T = [N(x)][G]\{u^e\} \quad = [\bar{N}(x)]\{u^e\}, \tag{4.24}$$

where $[\bar{N}(x)]$ is the shape function matrix for mechanical degrees of freedom and are given in Appendix-A. To obtain the stiffness matrix, forced boundary conditions (Equation-(4.15)) are used where, H_{xp} and (ΔT) terms are used to get the equivalent nodal force due to coil current and temperature rise respectively. Substituting the displacement field from Equation-(4.18), the force resultants in Equation-(4.15) can be written in terms of the unknown constants $\{C\}$ as

$$\{N \quad V \quad M\}^T = [\bar{G}]\{C\} + \{R\}. \tag{4.25}$$

Substituting the expression of $\{C\}$ from Equation-(4.23), Equation-(4.25) can be written as

$$\{N \quad V \quad M\}^T = [\bar{G}][G]\{u^e\} + \{R\}. \tag{4.26}$$

Evaluating Equation-(4.26) at $x = 0$ and $x = L$, we get the nodal load vector, $\{F\}$ in terms of nodal displacement $\{u^e\}$, which can be written as

$$\begin{aligned} \{F\} &= \{-N(0) \quad -V(0) \quad -M(0) \quad N(L) \quad V(L) \quad M(L)\}^T \\ &= \begin{bmatrix} \bar{G}G(x=0) \\ \bar{G}G(x=L) \end{bmatrix} \{u^e\} + \left\{ \begin{array}{c} \{R\}(x=0) \\ \{R\}(x=L) \end{array} \right\} \\ &= [K]\{u^e\} + \{R_T\}(\Delta T) + \sum_p \{R_I\} In_p, \end{aligned} \tag{4.27}$$

where $[K]$ is the element stiffness matrix. $\{R_T\}$ and $\{R_I\}$ are element load vector coefficient due to temperature rise and current actuation respectively. Explicit forms of $[K]$, $\{R_T\}$ and $\{R_I\}$ are given in Appendix A.

Next, the consistent element mass matrix $[M]$ is derived. It can be computed from the expression:

$$[M] = \int_0^L \int_A ([\hat{N}(x)]^T [\varrho][\hat{N}(x)]) dAdx, \tag{4.28}$$

where $[\hat{N}(x)]$ is another shape function, which can be calculated from longitudinal shape function $[\bar{N}(x)]$ as

$$[\hat{N}(x)] = \begin{bmatrix} 1 & 0 & -z \\ 0 & 0 & 0 \\ 0 & 1 & 0 \end{bmatrix} [\bar{N}(x)]. \tag{4.29}$$

The nonzero elements of the mass matrix are given in Appendix-A. Mass and stiffness matrices for conventional element can be calculated considering $\beta_e = 0$. After finite element solution, from the strain and the magnetic field, stress and magnetic flux density can be calculated using Equation-(4.3).

4.2.1.2 Coupled Formulation

For finite element beam formulation based on coupled constitutive model, magnetic field terms H_{xp} will be considered as an unknown variable. Hence, the governing equation and associated boundary condition related to this problem are given by Equation-(4.7) and Equation-(4.8) respectively. From Equation-(4.7) H_{xp} can be written as

$$H_{xp} = \left(-\frac{A^e_{11p}}{A^\epsilon_{\mu p}}u^\circ_{,x} + \frac{B^e_{11p}}{A^\epsilon_{\mu p}}w^\circ_{,xx} - In_p\frac{A^\sigma_{\mu p}}{A^\epsilon_{\mu p}} - (\Delta T)\frac{A^{e\alpha}_{11p}}{A^\epsilon_{\mu p}}\right). \tag{4.30}$$

Differentiating Equation-(4.30) with respect to x, we get

$$H_{xp,x} = \left(-\frac{A^e_{11p}}{A^\epsilon_{\mu p}}u^\circ_{,xx} + \frac{B^e_{11p}}{A^\epsilon_{\mu p}}w^\circ_{,xxx}\right), \tag{4.31}$$

and substituting this in Equations-(4.7), we get

$$\begin{aligned} \delta u^\circ : \quad & I_0\ddot{u}^\circ - I_1\ddot{w}^\circ_{,x} + A^*_{11}u^\circ_{,xx} - B^*_{11}w^\circ_{,xxx} = 0, \\ \delta w^\circ : \quad & I_0\ddot{w}^\circ + B^*_{11}u^\circ_{,xxx} - D^*_{11}w^\circ_{,xxxx} = 0, \end{aligned} \tag{4.32}$$

where A^*_{11}, B^*_{11} and D^*_{11} are

$$A^*_{11} = A_{11} + \sum_p \frac{{A^e_{11p}}^2}{A^\epsilon_{\mu p}},\; B^*_{11} = B_{11} + \sum_p \frac{A^e_{11p}B^e_{11p}}{A^\epsilon_{\mu p}},\; D^*_{11} = D_{11} + \sum_p \frac{{B^e_{11p}}^2}{A^\epsilon_{\mu p}}. \tag{4.33}$$

Similarly the boundary conditions given in Equation-(4.8) can be written as

$$\begin{aligned} N &= -A^*_{11}u^\circ_{,x} + B^*_{11}w^\circ_{,xx} + \sum_p In_pA^e_{11p}\frac{A^\sigma_{\mu p}}{A^\epsilon_{\mu p}} + A^{\alpha\star}_{11}\Delta T, \\ M &= B^*_{11}u^\circ_{,x} - D^*_{11}w^\circ_{,xx} - \sum_p In_pB^e_{11p}\frac{A^\sigma_{\mu p}}{A^\epsilon_{\mu p}} - B^{\alpha\star}_{11}\Delta T, \\ V &= -B^*_{11}u^\circ_{,xx} + D^*_{11}w^\circ_{,xxx}. \end{aligned} \tag{4.34}$$

The formulation of this element will proceed in a similar manner as the uncoupled case and the stiffness and mass matrices and the temperature and the current induced load vectors take the same form as uncoupled case with A_{11}, B_{11} and D_{11} replaced by $A^*_{11}, B^*_{11}, D^*_{11}$.

After calculating the mechanical displacement, the magnetic field can be obtained using Equation-(4.30).

4.2.2 FE Formulation for First Order Shear Deformable (Timoshenko) Beam

The displacement and magnetic field variation for a Timoshenko beam element is given by

$$\begin{aligned} U(x,y,t) &= u^\circ(x,t) - z\phi(x,t), \\ V(x,y,t) &= 0, \\ W(x,y,t) &= w^\circ(x,t), \\ H_x(x,y,t) &= H_{xp}(x,t), \end{aligned} \tag{4.35}$$

where ϕ is the rotation of the cross-section about Y axis. Using Equation-(4.35), the linear strains can be written as

$$\epsilon_{xx} = u^\circ_{,x} - z\phi_{,x} - \alpha\Delta T, \gamma_{xz} = -\phi + w^\circ_{,x}. \tag{4.36}$$

The constitutive relation for the beam with magnetostrictive patches is given by

$$\begin{aligned} \left\{ \begin{array}{c} \sigma_{xx} \\ \tau_{xz} \end{array} \right\} &= \left[\begin{array}{cc} \bar{Q}_{11} & \bar{Q}_{15} \\ \bar{Q}_{15} & \bar{Q}_{55} \end{array} \right] \left\{ \begin{array}{c} \varepsilon_{xx} \\ \gamma_{xz} \end{array} \right\} - \left\{ \begin{array}{c} e_{11} \\ e_{15} \end{array} \right\} H \ , \\ B_{xx} &= \left[\begin{array}{cc} e_{11} & e_{15} \end{array} \right] \left\{ \begin{array}{c} \varepsilon_{xx} \\ \gamma_{xz} \end{array} \right\} + \ \mu^\epsilon \ H \ , \end{aligned} \tag{4.37}$$

where γ_{xz} and τ_{xz}, are the shear strain and shear stress respectively. $\bar{Q}_{ij}$ is the material constant for mechanical loads, while e_{ij} and μ^ϵ are magnetostrictive stress coefficient and permeability at constant strain of the magnetostrictive material, respectively. The strain energy (S) considering shear strain is then given by

$$S = \frac{1}{2} \int_0^L \int_A (\sigma_{xx}\varepsilon_{xx} + \tau_{xz}\gamma_{xz})\, dA\, dx.$$

Other energy terms are of similar form as of the Euler-Bernoulli case, which is given in Equation-(4.5) and Equation-(4.6), respectively. Applying Hamilton's principle, the following differential equations of motion and their associated boundary conditions are obtained in terms of the three mechanical degrees of freedom (u°, w° and ϕ) and one magnetic degrees of freedom (H_{xp}). They are given by

$$\delta u^\circ : \quad I_0\ddot{u^\circ} - I_1\ddot{\phi} - A_{11}\frac{\partial^2 u^\circ}{\partial x^2} + B_{11}\frac{\partial^2 \phi}{\partial x^2} - A_{15}(\frac{\partial^2 w^\circ}{\partial x^2} - \frac{\partial \phi}{\partial x}) + \sum_p A^e_{11p}\frac{\partial H_{xp}}{\partial x} = 0 \, , \tag{4.38a}$$

$$\delta w^\circ : \quad I_0\ddot{w^\circ} - A_{55}(\frac{\partial^2 w^\circ}{\partial x^2} - \frac{\partial \phi}{\partial x}) - A_{15}\frac{\partial^2 u^\circ}{\partial x^2} + B_{15}\frac{\partial^2 \phi}{\partial x^2} + \sum_p A^e_{15p}\frac{\partial H_{xp}}{\partial x} = 0 \, , \tag{4.38b}$$

$$\delta \phi : \quad I_2\ddot{\phi} - I_1\ddot{u^\circ} + B_{11}\frac{\partial^2 u^\circ}{\partial x^2} - D_{11}\frac{\partial^2 \phi}{\partial x^2} - A_{55}(\frac{\partial w^\circ}{\partial x} - \phi) + B_{15}(\frac{\partial^2 w^\circ}{\partial x^2} - \frac{\partial \phi}{\partial x}) - \sum_p B^e_{11p}\frac{\partial H_{xp}}{\partial x} - A_{15}\frac{\partial u^\circ}{\partial x} + B_{15}\frac{\partial \phi}{\partial x} + \sum_p A^e_{15p}H_{xp} + A^\alpha_{15}(\Delta T) = 0 \, , \tag{4.38c}$$

$$\delta H_{xp} : \quad -A^e_{11p}\frac{\partial u^\circ}{\partial x} + B^e_{11p}\frac{\partial \phi}{\partial x} - A^e_{15p}(\frac{\partial w^\circ}{\partial x} - \phi) - A^\epsilon_{\mu p}H_{xp} + In_pA^\sigma_\mu + A^{e\alpha}_{11p}(\Delta T) = 0 \, , \tag{4.38d}$$

and the corresponding force boundary conditions are :

$$N = A_{11}\frac{\partial u^\circ}{\partial x} - B_{11}\frac{\partial \phi}{\partial x} + A_{15}(\frac{\partial w^\circ}{\partial x} - \phi) - \sum_p A^e_{11p}H_{xp} - A^\alpha_{11}(\Delta T) \, , \tag{4.39a}$$

$$M = -B_{11}\frac{\partial u^\circ}{\partial x} + D_{11}\frac{\partial \phi}{\partial x} - B_{15}(\frac{\partial w^\circ}{\partial x} - \phi) + \sum_p B^e_{11p}H_{xp} + B^\alpha_{11}(\Delta T) \, , \tag{4.39b}$$

$$V = A_{55}(\frac{\partial w^\circ}{\partial x} - \phi) + A_{15}\frac{\partial u^\circ}{\partial x} - B_{15}\frac{\partial \phi}{\partial x} - \sum_p A^e_{15p}H_{xp} - A^\alpha_{15}(\Delta T). \tag{4.39c}$$

If $\bar{Q}_{15} = 0$, we get $A_{15} = B_{15} = A^\alpha_{15} = 0$. Similarly considering $e_{15} = 0$ we get $A^e_{15p} = B^e_{15p} = 0$.

4.2.2.1 Uncoupled Formulation

For finite element beam formulation based on uncoupled constitutive model, we have $H_{xp} = H = nI, \partial H_{xp}/\partial x = 0$. Hence, the governing equation and the associated boundary condition become

$$\begin{aligned}
\delta u^\circ : \quad & I_0\ddot{u}^\circ - I_1\ddot{\phi} - A_{11}\frac{\partial^2 u^\circ}{\partial x^2} + B_{11}\frac{\partial^2 \phi}{\partial x^2} = 0 \ , \\
\delta w^\circ : \quad & I_0\ddot{w}^\circ - A_{55}(\frac{\partial^2 w^\circ}{\partial x^2} - \frac{\partial \phi}{\partial x}) = 0 \ , \\
\delta \phi : \quad & I_2\ddot{\phi} - I_1\ddot{u}^\circ + B_{11}\frac{\partial^2 u^\circ}{\partial x^2} - D_{11}\frac{\partial^2 \phi}{\partial x^2} - A_{55}(\frac{\partial w^\circ}{\partial x} - \phi) = 0 \ ,
\end{aligned} \tag{4.40}$$

and

$$\begin{aligned}
N &= A_{11}\frac{\partial u^\circ}{\partial x} - B_{11}\frac{\partial \phi}{\partial x} - \sum_p A^e_{11p}H_{xp} - A^\alpha_{11}(\Delta T) \ , \\
M &= -B_{11}\frac{\partial u^\circ}{\partial x} + D_{11}\frac{\partial \phi}{\partial x} + \sum_p B^e_{11p}H_{xp} + B^\alpha_{11}(\Delta T) \ , \\
V &= A_{55}(\frac{\partial w^\circ}{\partial x} - \phi).
\end{aligned} \tag{4.41}$$

Similar to the Euler-Bernoulli beam, the magnetic field will appear only in the force boundary conditions.

The FE equation begins by solving the static part of equation (4.40) exactly. The solution is given by

$$u^\circ = c_1 + c_2 x + c_3 x^2 \ , \tag{4.42a}$$

$$w^\circ = c_4 + c_5 x + c_6 x^2 + c_7 x^3 \ , \tag{4.42b}$$

$$\phi = c_8 + c_9 x + c_{10} x^2, \tag{4.42c}$$

where $c_1, .., c_{10}$ are the ten unknown constants to be determined from six degrees of freedom (u°, w°, ϕ at the two nodes). Hence, there are only six independent constants and four dependent constants, which can be obtained by substituting Equation-(4.42) in the static part of the Equation-(4.40). The formulation of the stiffness matrix, mass matrix, thermal load vector and current load vector can be carried out in a similar fashion as shown in the case of Euler-Bernoulli beam. These matrices are given in Appendix-B.

4.2.2.2 Coupled Formulation

For finite element beam formulation based on coupled constitutive model, magnetic field terms H_{xp} will be considered as an unknown variable. From Equation-(4.38d), H_{xp} can be written as

$$H_{xp} = \frac{1}{A^\epsilon_{\mu p}}\left[-A^e_{11p}\frac{\partial u}{\partial x} + B^e_{11p}\frac{\partial \phi}{\partial x} - A^e_{15p}(\frac{\partial w}{\partial x} - \phi) + In_p A^\sigma_{\mu p} + A^{e\alpha}_{11p}(\Delta T)\right] \ . \tag{4.43}$$

Differentiating Equation-(4.43) with respect to x, we get

$$H_{xp,x} = \frac{1}{A^{\epsilon}_{\mu p}}\left[-A^{e}_{11p}\frac{\partial^2 u}{\partial x^2} + B^{e}_{11p}\frac{\partial^2 \phi}{\partial x^2} - A^{e}_{15p}(\frac{\partial^2 w}{\partial x^2} - \frac{\partial \phi}{\partial x})\right] . \tag{4.44}$$

Now substituting $H_{xp,x}$ in Equations-(4.38a-4.38c), we get

$$\delta u: \quad -A^{\star}_{11}\frac{\partial^2 u}{\partial x^2} + B^{\star}_{11}\frac{\partial^2 \phi}{\partial x^2} - A^{\star}_{15}\left(\frac{\partial^2 w}{\partial x^2} - \frac{\partial \phi}{\partial x}\right) = 0, \tag{4.45a}$$

$$\delta w: \quad -A^{\star}_{55}(\frac{\partial^2 w}{\partial x^2} - \frac{\partial \phi}{\partial x}) - A^{\star}_{15}\frac{\partial^2 u}{\partial x^2} + B^{\star}_{15}\frac{\partial^2 \phi}{\partial x^2} = 0, \tag{4.45b}$$

$$\begin{aligned}\delta \phi: \quad & B^{\star}_{11}\frac{\partial^2 u}{\partial x^2} - D^{\star}_{11}\frac{\partial^2 \phi}{\partial x^2} - A^{\star}_{55}(\frac{\partial w}{\partial x} - \phi) + B^{\star}_{15}(\frac{\partial^2 w}{\partial x^2} - \frac{\partial \phi}{\partial x}) \\ & -A^{\star}_{15}\frac{\partial u}{\partial x} + B^{\star}_{15}\frac{\partial \phi}{\partial x} + A^{I\alpha}_{15} = 0,\end{aligned} \tag{4.45c}$$

and similarly boundary conditions from Equations-(4.39a-4.39c) will be

$$N = A^{\star}_{11}\frac{\partial u}{\partial x} - B^{\star}_{11}\frac{\partial \phi}{\partial x} + A^{\star}_{15}(\frac{\partial w}{\partial x} - \phi) - \sum_p A^{e}_{11p}\frac{A^{\sigma}_{\mu p}}{A^{\epsilon}_{\mu p}}In_p - A^{\alpha\star}_{11}(\Delta T) , \tag{4.46a}$$

$$M = -B^{\star}_{11}\frac{\partial u}{\partial x} + D^{\star}_{11}\frac{\partial \phi}{\partial x} - B^{\star}_{15}(\frac{\partial w}{\partial x} - \phi) + \sum_p B^{e}_{11p}\frac{A^{\sigma}_{\mu p}}{A^{\epsilon}_{\mu p}}In_p + B^{\alpha\star}_{11}(\Delta T) , \tag{4.46b}$$

$$V = A^{\star}_{55}(\frac{\partial w}{\partial x} - \phi) + A^{\star}_{15}\frac{\partial u}{\partial x} - B^{\star}_{15}\frac{\partial \phi}{\partial x} - \sum_p A^{e}_{15p}\frac{A^{\sigma}_{\mu p}}{A^{\epsilon}_{\mu p}}In_p - A^{\alpha\star}_{15}(\Delta T) , \tag{4.46c}$$

where A^{*}_{ij}, B^{*}_{ij} , $D^{*}_{ij}, A^{\alpha\star}_{ij}$ and $B^{\alpha\star}_{ij}$ can be written as

$$\begin{aligned}A^{*}_{11} &= A_{11} + \sum_p \frac{A^{e}_{11p}A^{e}_{11p}}{A^{\epsilon}_{\mu p}}, \quad A^{*}_{15} = A_{15} + \sum_p \frac{A^{e}_{15p}A^{e}_{11p}}{A^{\epsilon}_{\mu p}}, \quad A^{*}_{55} = A_{55} + \sum_p \frac{A^{e}_{15p}A^{e}_{15p}}{A^{\epsilon}_{\mu p}}, \\ B^{*}_{11} &= B_{11} + \sum_p \frac{A^{e}_{11p}B^{e}_{11p}}{A^{\epsilon}_{\mu p}}, \quad B^{*}_{15} = B_{15} + \sum_p \frac{B^{e}_{11p}A^{e}_{15p}}{A^{\epsilon}_{\mu p}}, \quad D^{*}_{11} = D_{11} + \sum_p \frac{B^{e}_{11p}B^{e}_{11p}}{A^{\epsilon}_{\mu p}}, \\ A^{\alpha\star}_{11} &= A^{\alpha}_{11} + \sum_p \frac{A^{e\alpha}_{11p}A^{e}_{11p}}{A^{\epsilon}_{\mu p}}, \quad B^{\alpha\star}_{11} = B^{\alpha}_{11} + \sum_p \frac{A^{e\alpha}_{11p}B^{e}_{11p}}{A^{\epsilon}_{\mu p}}, \quad A^{\alpha\star}_{15} = A^{\alpha}_{15} + \sum_p \frac{A^{e}_{15p}A^{e\alpha}_{11p}}{A^{\epsilon}_{\mu p}}.\end{aligned} \tag{4.47}$$

For superconvergent formulation of the element, governing differential Equation-(4.45) should be homogenous. To get the homogeneous governing differential equations, the last term of Equation-(4.45c) given by

$$A^{I\alpha}_{15} = A^{\alpha}_{15}(\Delta T) + \sum_p \frac{1}{A^{\epsilon}_{\mu p}}A^{e}_{15p}A^{\sigma}_{\mu p}In_p, \tag{4.48}$$

should be zero. The first term of Equation-(4.48)($A^{\alpha}_{15}(\Delta T)$) will vanish if $\bar{Q}_{15} = 0$ or $\Delta T = 0$, and similarly the second term ($\frac{1}{A^{\epsilon}_{\mu}} A^{e}_{15} A^{\sigma}_{\mu} In$) will vanish if $e_{15} = 0$ or $In_p = 0$.

To get the polynomial order of the unknown variables, equations of single variable is required, which can be obtained after substituting these homogenous equations. These single variable equations are derived in the following manner. Equating $(w^{\circ}_{,xx} - \phi_{,x})$ from Equation-(4.45a) and Equation-(4.45b), we can write

$$\frac{\partial^2 u^{\circ}}{\partial x^2} = \alpha_1 \frac{\partial^2 \phi}{\partial x^2} \tag{4.49}$$

where α_1 is

$$\alpha_1 = \frac{A^{\star}_{55} B^{\star}_{11} - A^{\star}_{15} B^{\star}_{15}}{A^{\star}_{11} A^{\star}_{55} - A^{\star}_{15} A^{\star}_{15}} \tag{4.50}$$

Differentiating Equation-(4.45a) with respect to x and using Equation-(4.49), Equation-(4.45b) can be written as

$$\alpha_2 \frac{\partial^3 \phi}{\partial x^3} = 0, \quad \frac{\partial^3 u}{\partial x^3} = 0, \qquad \frac{\partial^4 w}{\partial x^4} = 0, \qquad \frac{\partial^3 H_{xp}}{\partial x^3} = 0, \tag{4.51}$$

where α_2 is

$$\alpha_2 = \alpha_1 B^{\star}_{11} - D^{\star}_{11} - \alpha_1 \frac{B^{\star}_{15} A^{\star}_{15}}{A^{\star}_{55}} + \frac{B^{\star}_{15} B^{\star}_{15}}{A^{\star}_{55}} \tag{4.52}$$

From Equation-(4.51), we can evaluate the exact polynomial order of mid plane displacement and it takes the same form as given for uncoupled formulation, which is given in Equation-(4.42). Formulation can be proceeded on similar lines as the previous case.

4.3 Numerical Experiments.

The objective of this section is to bring out the effect of super convergent property of the formulated elements (Super convergent Euler-Bernoulli (ScEB) and Super convergent First order Shear Deformable (ScFSDT) elements) on the overall response of a composite beam with magnetostrictive patches. The results of the formulated elements are compared with 2-D FEM formulation, the conventional Euler-Bernoulli (CEB), conventional first order shear deformable theory with full integration (CFSDT) and reduced integrated first order Shear deformable theory (RIFSDT). Here, I have demonstrated the super-convergent properties in static, free vibration and dynamic response problems. Before I proceed with the numerical experiment, we first write the cross sectional properties in a simplified form. For numerical calculation, the thermal expansion coefficient α, permeability μ and stress coefficient of magnetostriction e, are assumed same through out the thickness of the individual magnetostrictive layer, and A^e_{11p}, B^e_{11p} and $A^\epsilon_{\mu p}$ can be calculated from Equations-(4.10,4.12) as:

$$A^e_{ijp} = e_{ij}(z_{tp} - z_{bp}), \quad B^e_{ijp} = \frac{e_{ij}}{2}(z^2_{tp} - z^2_{bp}), \quad A^\epsilon_{\mu p} = \mu_\epsilon(z_{tp} - z_{bp}), \tag{4.53}$$

where z_{tp} and z_{bp} are the distance of the top and bottom of the layer p from the neutral axis. Now, $A^\star_{11}$, $B^\star_{11}$ and $D^\star_{11}$ can be calculated from Equations-(4.33)as:

$$\begin{aligned}
A^\star_{11} &= A_{11} + \sum_p \frac{{A^e_{11p}}^2}{A^\epsilon_{\mu p}} = A_{11} + \sum_p \frac{e^2_{11}}{\mu_\epsilon}(z_{tp} - z_{bp}),\\
B^\star_{11} &= B_{11} + \sum_p \frac{A^e_{11p}B^e_{11p}}{A^\epsilon_{\mu p}} = B_{11} + \sum_p \frac{e^2_{11}}{2\mu_\epsilon}(z^2_{tp} - z^2_{bp}),\\
D^\star_{11} &= D_{11} + \sum_p \frac{B^e_{11p}B^e_{11}}{A^\epsilon_{\mu p}} = D_{11} + \sum_p \frac{e^2_{11}}{4\mu_\epsilon}\frac{(z^2_{tp} - z^2_{bp})^2}{z_{tp} - z_{pb}}.
\end{aligned} \tag{4.54}$$

However, as the magnetic field in thickness direction is considered as constant throughout the magnetostrictive layer, the analysis will give a constraint result. To overcome this effect, we can consider this layer as infinite numbers of magnetostrictive sub-layers and each sub-layer is added to obtain the corresponding coupling stiffness. Hence the, above equation can be written as:

$$\begin{aligned}
A^\star_{11} &= A_{11} + \sum_p \left(\frac{e^2}{\mu_\epsilon}\sum_i (z_{i+1} - z_i)\right) = A_{11} + \sum_p \frac{e^2}{\mu_\epsilon}(z_{tp} - z_{bp}),\\
B^\star_{11} &= B_{11} + \sum_p \left(\frac{e^2}{2\mu_\epsilon}\sum_i (z^2_{i+1} - z^2_i)\right) = B_{11} + \sum_p \frac{e^2}{2\mu_\epsilon}(z^2_{tp} - z^2_{bp}),\\
D^\star_{11} &= D_{11} + \sum_p \left(\frac{e^2}{4\mu_\epsilon}\sum_i \frac{(z^2_{i+1} - z^2_i)^2}{z_{i+1} - z_i}\right) = D_{11} + \sum_p \frac{e^2}{3\mu_\epsilon}(z^3_{tp} - z^3_{bp}),
\end{aligned}$$

where z_{i+1} and z_i are the distance of top and bottom of the sub-layer from neutral axis. It is shown that due to an infinite sub-layer consideration only $D^\star_{11}$ value is changing from its earlier value given in Equation-(4.54). Similarly, other coefficients given in Equation-(4.47) can be written as:

$$A^\star_{15} = A_{15} + \sum_p \frac{A^e_{15p}A^e_{11p}}{A^\epsilon_{\mu p}} = A_{15} + \sum_p \frac{e_{15}e_{11}}{\mu_\epsilon}(z_{tp} - z_{bp}),$$

$$B_{15}^{\star} = B_{15} + \sum_p \frac{A_{15p}^e B_{11p}^e}{A_{\mu p}^{\epsilon}} = B_{15} + \sum_p \frac{e_{15} e_{11}}{2\mu_{\epsilon}}(z_{tp}^2 - z_{bp}^2),$$

$$A_{55}^{\star} = A_{55} + \sum_p \frac{{A_{15p}^e}^2}{A_{\mu p}^{\epsilon}} = A_{15} + \sum_p \frac{e_{15}^2}{\mu_{\epsilon}}(z_{tp} - z_{bp}),$$

$$A_{11}^{\alpha\star} = A_{11}^{\alpha} + \sum_p \frac{A_{11p}^e A_{11p}^{\alpha e}}{A_{\mu p}^{\epsilon}} = A_{11}^{\alpha} + \sum_p \frac{\alpha e_{11}^2}{\mu_{\epsilon}}(z_{tp} - z_{bp}),$$

$$B_{11}^{\alpha\star} = B_{11}^{\alpha} + \sum_p \frac{B_{11p}^e A_{11p}^{\alpha e}}{A_{\mu p}^{\epsilon}} = B_{11}^{\alpha} + \sum_p \frac{\alpha e_{11}^2}{2\mu_{\epsilon}}(z_{tp}^2 - z_{bp}^2),$$

$$A_{15}^{\alpha\star} = A_{15}^{\alpha} + \sum_p \frac{A_{15p}^e A_{11p}^{\alpha e}}{A_{\mu p}^{\epsilon}} = A_{15}^{\alpha} + \sum_p \frac{\alpha e_{11} e_{15}}{\mu_{\epsilon}}(z_{tp} - z_{bp}).$$

4.3.1 Static Analysis

Here we consider a cantilever beam with generalized lay up sequence shown in Figure-4.1. Single element closed form solution for static tip deflection of a cantilever composite beam with magnetostrictive patches subjected to tip vertical load, temperature rise and applied actuation current, is studied for both Euler-Bernoulli and Timoshenko beam model.

4.3.1.1 Euler-Bernoulli Beam

Tip deflection of the superconvergent coupled Euler-Bernoulli beam due to tip load F_Z $(\Delta T = 0, In_p = 0)$ is given by

$$w^{\circ} = -1/3 \frac{A_{11}^{\star} L^3}{{B_{11}^{\star}}^2 - A_{11}^{\star} D_{11}^{\star}} F_Z. \tag{4.55}$$

Similarly for conventional coupled Euler-Bernoulli finite element beam deflection, which was reported in last chapter, is given by

$$w^{\circ} = 1/12 \frac{\left(4 A_{11}^{\star} D_{11}^{\star} - {B_{11}^{\star}}^2\right) L^3 F_Z}{D_{11}^{\star}\left(-{B_{11}^{\star}}^2 + A_{11}^{\star} D_{11}^{\star}\right)}. \tag{4.56}$$

This above expression of tip deflection for CEB beam element for asymmetric lay up sequence can be derived similar way considering $\beta_e = 0$ given in Equation-(4.18). For

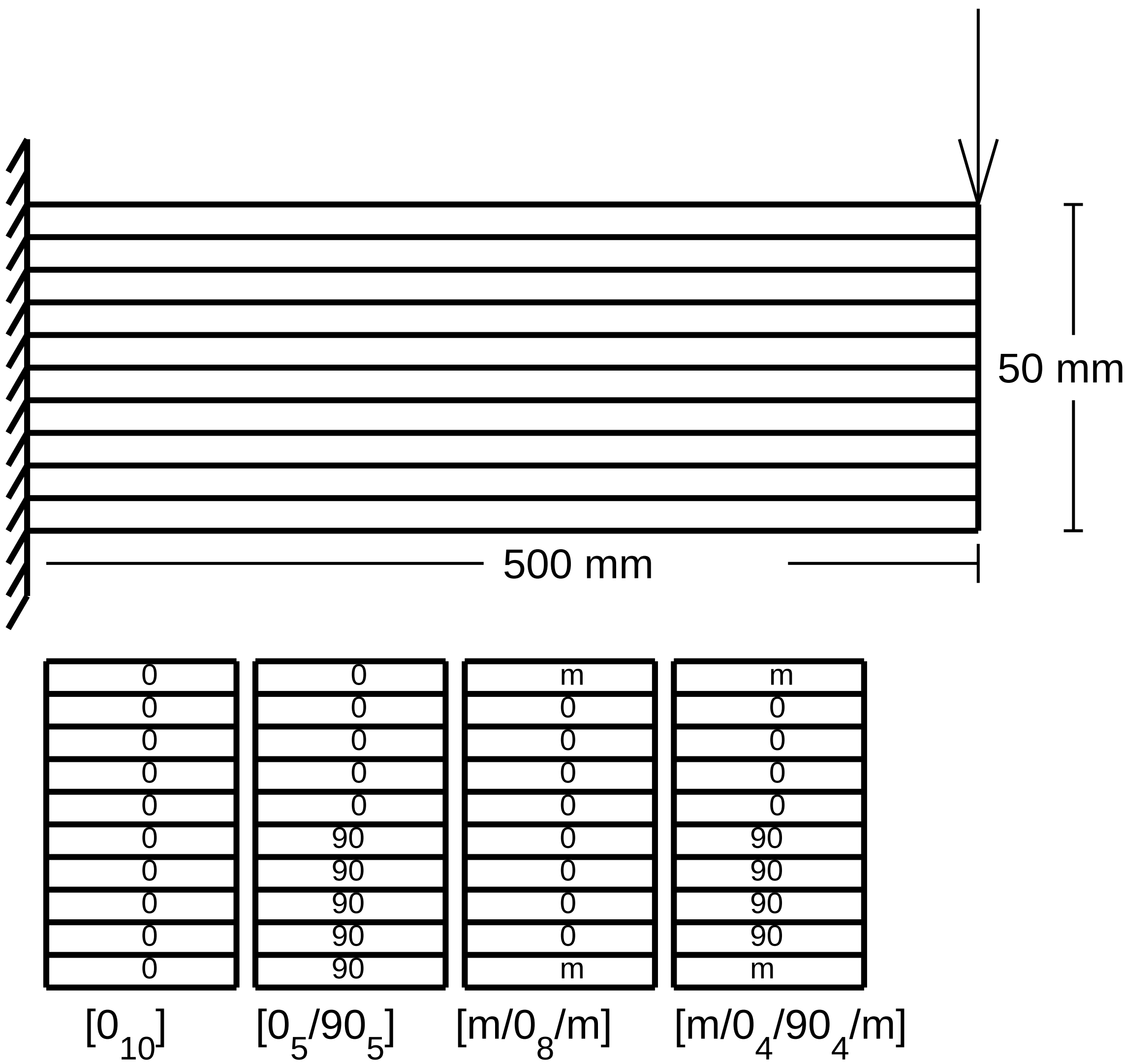

Figure 4.1: 10 layer composite cantilever beam with different layup sequence

$B^\star_{11} = 0$, both the results are same. The ratio of tip deflections of the superconvergent solution of the present element and the conventional element due to tip vertical load is given by

$$\frac{4A^\star_{11}D^\star_{11}}{4A^\star_{11}D^\star_{11} - {B^\star_{11}}^2}. \tag{4.57}$$

Next we will consider a case, where we have both coil current (In_p) and temperature rise (ΔT) (with out any tip load, $F_Z = 0$). Tip deflections for both the formulations are same for current and temperature load. The tip deflections due to both superconvergent and conventional formulations are given by

$$\left\{\begin{array}{c} u^\circ \\ w^\circ \\ \phi \end{array}\right\} = \frac{1}{({B^\star_{11}}^2 - A^\star_{11}\, D^\star_{11})} \sum_p \left\{\begin{array}{c} -L\left(-D^\star_{11}\, A^e_{11p}\, r + B^\star_{11}\, B^e_{11p}\, r\right) \\ -1/2\, L^2\left(-B^\star_{11}\, A^e_{11p}\, r + A^\star_{11}\, B^e_{11p}\, r\right) \\ -L\left(-B^\star_{11}\, A^e_{11p}\, r + A^\star_{11}\, B^e_{11p}\, r\right) \end{array}\right\} In_p$$
$$+\frac{1}{({B^\star_{11}}^2 - A^\star_{11}\, D^\star_{11})} \left(\left\{\begin{array}{c} -B^\star_{11} L B^{\alpha\star}_{11} \\ -1/2\, L^2 A^{\alpha\star}_{11} B^\star_{11} \\ -L A^{\alpha\star}_{11} B^\star_{11} \end{array}\right\} + \left\{\begin{array}{c} D^\star_{11}\, L A^{\alpha\star}_{11} \\ 1/2\, L^2 A^\star_{11} B^{\alpha\star}_{11} \\ L A^\star_{11} B^{\alpha\star}_{11} \end{array}\right\}\right)(\Delta T). \quad (4.58)$$

Ratio between tip deflection and tip slope for temperature rise or actuation current is given by

$$\frac{w^\circ}{\phi} = \frac{L}{2}$$

One interesting observation is if $A^\star_{11} B^{\alpha\star}_{11} = B^\star_{11} A^{\alpha\star}_{11}$, irrespective of the thermal coefficient distribution along the depth, beam will remain straight under temperature rise. Similar effect will happen for actuation current if $A^\star_{11} B^e_{11p} = B^\star_{11} A^e_{11p}$.

4.3.1.2 Timoshenko Beam

Tip deflection of the superconvergent coupled Timoshenko beam due to tip load F_Z is given by

$$w^\circ = \frac{\left(A^\star_{11} D^\star_{11} - 3A^\star_{11} L^2 \psi A_{55} - {B^\star_{11}}^2\right) L F_Z}{6A_{55}\left\{(14\psi - 1)(A^\star_{11} D^\star_{11} - {B^\star_{11}}^2) + A^\star_{11} L^2 \psi A_{55}\right\}}, \quad (4.59)$$

where $\psi = 1/(12 + L^2\beta_f)$. Similarly, the deflection at the tip of the single element cantilever beam for conventional (RIFSDT) element with linear shape function is given by

$$w^\circ = 4\frac{\left(A^\star_{11} A_{55} L^2 + 3A^\star_{11} D^\star_{11} - 3{B^\star_{11}}^2\right) L}{A_{55}\left(-12{B^\star_{11}}^2 + A^\star_{11} A_{55} L^2 + 12A^\star_{11} D^\star_{11}\right)} F_Z. \quad (4.60)$$

Tip deflection due to applied current and temperature rise in ScFSDT beam is given by

$$\begin{aligned} u^\circ \;=\; & \sum_p -\frac{Lr\left\{(1-14\psi)(B^\star_{11} B^e_{11p} - D^\star_{11} A^e_{11p}) + L^2 \psi A_{55} A^e_{11p}\right\}}{(14\psi - 1)(A^\star_{11} D^\star_{11} - {B^\star_{11}}^2) + A^\star_{11} L^2 \psi A_{55}} In_p \\ & - \frac{L\left\{(1-14\psi)(B^\star_{11} B^{\alpha\star}_{11} - D^\star_{11} A^{\alpha\star}_{11}) + L^2 \psi A_{55} A^{\alpha\star}_{11}\right\}}{(14\psi - 1)(A^\star_{11} D^\star_{11} - {B^\star_{11}}^2) + A^\star_{11} L^2 \psi A_{55}} (\Delta T), \end{aligned}$$

$$
\begin{aligned}
w^{\circ} &= \sum_{p} \frac{L^2 r(1-21\psi)(B^{\star}_{11}A^{e}_{11p} - A^{\star}_{11}B^{e}_{11p})}{3\left((14\psi-1)(A^{\star}_{11}D^{\star}_{11} - {B^{\star}_{11}}^2) + A^{\star}_{11}L^2\psi A_{55}\right)} In_p \\
&+ \frac{L^2(1-21\psi)(B^{\star}_{11}A^{\alpha\star}_{11} - A^{\star}_{11}B^{\alpha\star}_{11})}{3\left((14\psi-1)(A^{\star}_{11}D^{\star}_{11} - {B^{\star}_{11}}^2) + A^{\star}_{11}L^2\psi A_{55}\right)}(\Delta T),
\end{aligned}
$$

$$
\begin{aligned}
\phi &= \sum_{p} \frac{Lr(1-14\psi)(B^{\star}_{11}A^{e}_{11p} - A^{\star}_{11}B^{e}_{11p})}{(14\psi-1)(A^{\star}_{11}D^{\star}_{11} - {B^{\star}_{11}}^2) + A^{\star}_{11}L^2\psi A_{55}} In_p \\
&+ \frac{L(1-14\psi)(B^{\star}_{11}A^{\alpha\star}_{11} - A^{\star}_{11}B^{\alpha\star}_{11})}{(14\psi-1)(A^{\star}_{11}D^{\star}_{11} - {B^{\star}_{11}}^2) + A^{\star}_{11}L^2\psi A_{55}}(\Delta T).
\end{aligned}
$$

Ratio between tip deflection and tip slope for temperature rise or actuation current is given by

$$\frac{w^{\circ}}{\phi} = \frac{L(1-21\psi)}{3(1-14\psi)}$$

Similar to Euler-Bernoulli formulation, if $A^{\star}_{11}B^{\alpha\star}_{11} = B^{\star}_{11}A^{\alpha\star}_{11}$, irrespective of the thermal coefficient distribution along the depth, beam will remain straight under temperature rise. This effect will also be observed for actuation current, if $A^{\star}_{11}B^{e}_{11p} = B^{\star}_{11}A^{e}_{11p}$.

4.3.1.3 Single Element Performance for Static Analysis

In this section, single element solution of static tip deflection and first three natural frequencies are obtained for a 500 mm long 50 mm thick cantilever composite beam with different lay up sequences (which is shown in Figure-4.1). Elastic modulus of composite is taken as 181 GPa and 10.3 GPa in parallel and perpendicular direction of the fiber. Poisson's ratio, density and shear modulus of composite is assumed as 0.0, 1600 kg/m^3 and 28 GPa respectively. Elastic modulus, Poisson's ratio, shear modulus and density of the magnetostrictive material is assumed as 30 GPa, 0.0, 23 GPa and 9250 kg/m^3 respectively. Magneto-mechanical coupling coefficient is taken as $15X10^{-9}$ m/amp. Results are compared with 2-D plane strain finite element solution taking 100X10, four noded quadratic elements. Single element RIFSDT results are also compared with the super convergent and 2-D FEM results. Static tip deflections are calculated for tip vertical load of 1 kN. Table-(4.1) shows the tip deflection for tip vertical load of $[0_{10}]$ and $[0_5/90_5]$ lay up sequence. For symmetric layup sequence ($[0_{10}]$), formulation of ScEB and CEB are same hence their results are within 1.8% error. Here CFSDT, which is first order shear deformable element with full integration, is giving absurd result of 94% error. RIFSDT is showing 24.7% error and ScFSDT is within 0.2% error. Similarly for asymmetric layup

Table 4.1: Tip Deflection (mm) for Static Tip Load of 1 kN

	$[0_{10}]$	$[0_5/90_5]$
CEB	0.442 (1.8 %)	1.766 (15.3 %)
ScEB	0.442 (1.8 %)	2.076 (0.5%)
CFSDT	0.027 (94 %)	0.028 (98.7%)
ScFSDT	0.449 (0.2 %)	2.083 (0.1%)
RIFSDT	0.339 (24.7 %)	1.564 (25%)
2D FEM	0.450 (0 %)	2.086 (0 %)

sequence ($[0_5/90_5]$), CFSDT is giving an error of 98%. RIFSDT is showing 25% error and ScFSDT is within 0.2% error. Table-(4.2) shows the tip deflection for $[m/0_8/m]$ and

Table 4.2: Tip Deflection (mm) for Static Tip Load of 1 kN

	$[m/0_8/m]$	$[m/0_4/90_4/m]$
CEB uncoupled	0.746 (1.3%)	1.959 (11%)
ScEB uncoupled	0.746 (1.3%)	2.192 (0.4%)
CFSDT uncoupled	0.029 (96%)	0.293 (86.7%)
ScFSDT uncoupled	0.753 (0.4%)	2.200 (0.05%)
RIFSDT uncoupled	0.567 (25 %)	1.652 (25%)
2D FEM uncoupled	0.756 (0 %)	2.201 (0%)
CEB coupled	0.644 (1.3%)	1.327 (8.3%)
ScEB coupled	0.644 (1.3%)	1.439 (0.6%)
CFSDT coupled	0.029 (95.6%)	0.292 (80%)
ScFSDT coupled	0.651 (0.3%)	1.446 (0.07%)
RIFSDT coupled	0.490 (25%)	1.088 (24.8%)
2D FEM coupled	0.653 (0%)	1.447 (0%)

$[m/0_4/90_4/m]$ lay up sequence for both coupled and uncoupled formulation. Here for both coupled and uncoupled ScFSDT formulation, error in tip deflection is within 0.5 and 0.1% in $[m/0_8/m]$ and $[m/0_4/90_4/m]$ layup sequence respectively. For uncoupled formulation ($[m/0_4/90_4/m]$) CEB is giving 11% error. These errors for ScEB formulation are 1.3 and 0.6%. Super convergent formulation is giving less than 2.0% error, RIFSDT is giving 25% error and CFSDT is above 80% error. Table-(4.3) shows the tip deflection for tip vertical load for a beam with $[m/0_8/m]$ and $[m/0_4/90_4/m]$ lay up sequence for both coupled and uncoupled analysis. Static tip deflections are calculated for coil current of 1.0 ampere with 20000 turn/m coil turns. As the difference between conventional and ScEB beam is on vertical deflection for vertical load, results are same for actuation current, which gives axial load and moment. Again, conventional FSDT gives absurd result.

Table 4.3: Tip Deflection (mm) for Actuation Current

	$[m/0_8/m]$	$[m/0_4/90_4/m]$
CEB uncoupled	0.1132	0.2105
ScEB uncoupled	0.1132	0.2105
CFSDT uncoupled	0.0043	0.0028
ScFSDT uncoupled	0.1132	0.2105
RIFSDT uncoupled	0.1132	0.2105
2D FEM uncoupled	0.1131	0.2106
CEB coupled	0.2112	0.3120
ScEB coupled	0.2112	0.3120
CFSDT coupled	0.0093	0.0063
ScFSDT coupled	0.2112	0.3120
RIFSDT coupled	0.2112	0.3124
2D FEM coupled	0.2109	0.3115

The results are showing that single super convergent element for both ScEB and ScFSDT assumption is sufficient to get the tip deflection of the beam for tip vertical load with in 2.0% error. Single element CFSDT is giving absurd result (error of 94-95%) due to linear shape function use in element formulation even for thick beam. As the Euler Bernoulli (EB) assumption is stiffer than FSDT assumption, error in ScEB formulation (1.8%) is more than ScFSDT formulation (0.5%) and this difference is more for thicker beams.

4.3.2 Free Vibration Analysis.

4.3.2.1 Single Element Analysis.

Table-(4.4) shows the natural frequencies for $[0_{10}]$ and $[0_5/90_5]$ lay up sequence. First natural frequency for all the formulations is reasonable except for the conventional FSDT. Second and third natural frequencies of the beam are best for ScFSDT and ScEB formulations. Table-(4.5) shows the natural frequencies for $[m/0_8/m]$ and $[m/0_4/90_4/m]$ lay up sequence for both coupled and uncoupled analysis. First natural frequency for all the formulations is reasonable except for the conventional FSDT. Second and third natural frequencies are best for ScFSDT and ScEB formulations, when compared to 2-D FEM results.

Table 4.4: First Three Natural Frequencies (Hz)

	$[0_{10}]$			$[0_5/90_5]$		
CEB	344	3321	5864	180	2033	4460
ScEB	344	3321	5864	159	1510	4302
CFSDT	1179	5864	46541	1157	4254	46367
ScFSDT	341	3241	5864	158	1502	4303
RIFSDT	334	5864	3E18	155	4253	40237
2D FEM	338	1940	4865	157	948	2505

Table 4.5: First Three Natural Frequencies (Hz)

	$[m/0_8/m]$			$[m/0_4/90_4/m]$		
CEB uncoupled	189	1799	3827	121	1240	2899
ScEB uncoupled	189	1799	3827	110	1041	2845
CFSDT uncoupled	820	3827	24972	812	2828	24923
ScFSDT uncoupled	188	1772	3827	110	1036	2845
RIFSDT uncoupled	185	3827	16E14	108	2828	21631
2D FEM uncoupled	187	1087	2758	110	659	1740
CEB coupled	204	1937	3914	145	1435	3011
ScEB coupled	204	1937	3914	136	1286	2961
CFSDT coupled	822	3914	24991	814	2945	24942
ScFSDT coupled	202	1903	3914	136	1276	2962
RIFSDT coupled	298	3914	53E5	133	2945	21654
2D FEM coupled	200	1116	2940	135	808	2116

4.3.3 Super convergence Study.

4.3.3.1 Free Vibration Analysis.

Figure-4.2 shows the percentage errors of the first 10 natural frequencies of $[0_{10}]$ layup sequence. Here we have compared the natural frequencies for RIFSDT, ScFSDT, CEB (CEB and ScEB are same for symmetric layup sequence), FSDT Full (CFSDT) and 2-D FEM formulation. For first seven natural frequencies, 10 ScFSDT elements give better result than 20 RIFSDT elements. This shows the super convergence properties of the ScFSDT elements. The 8^{th}, 9^{th} and 10^{th} natural frequencies for 20 elements RIFSDT gives little better result than 10 elements ScFSDT. Figure-4.3 shows the percentage errors of the first 10 natural frequencies of $[0_5/90_5]$ layup sequence. Here all first 10 natural frequencies 10 ScFSDT elements give better result than 20 RIFSDT elements. Similarly 10 ScEB elements give better result than 20 CEB elements. This shows that asymmetric layup sequence exhibit a greater level of super convergence property. 20 elements FSDT

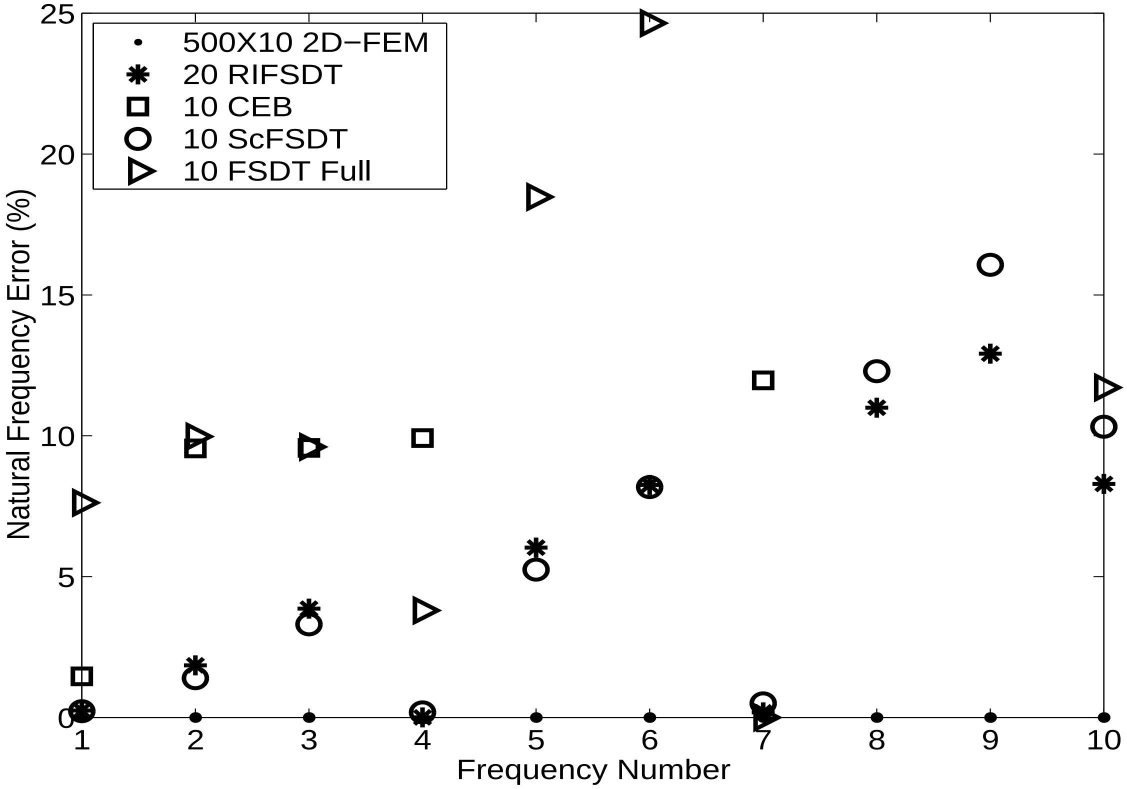

Figure 4.2: Natural Frequency for Cantilever Beam with $[0_{10}]$ Layup sequence

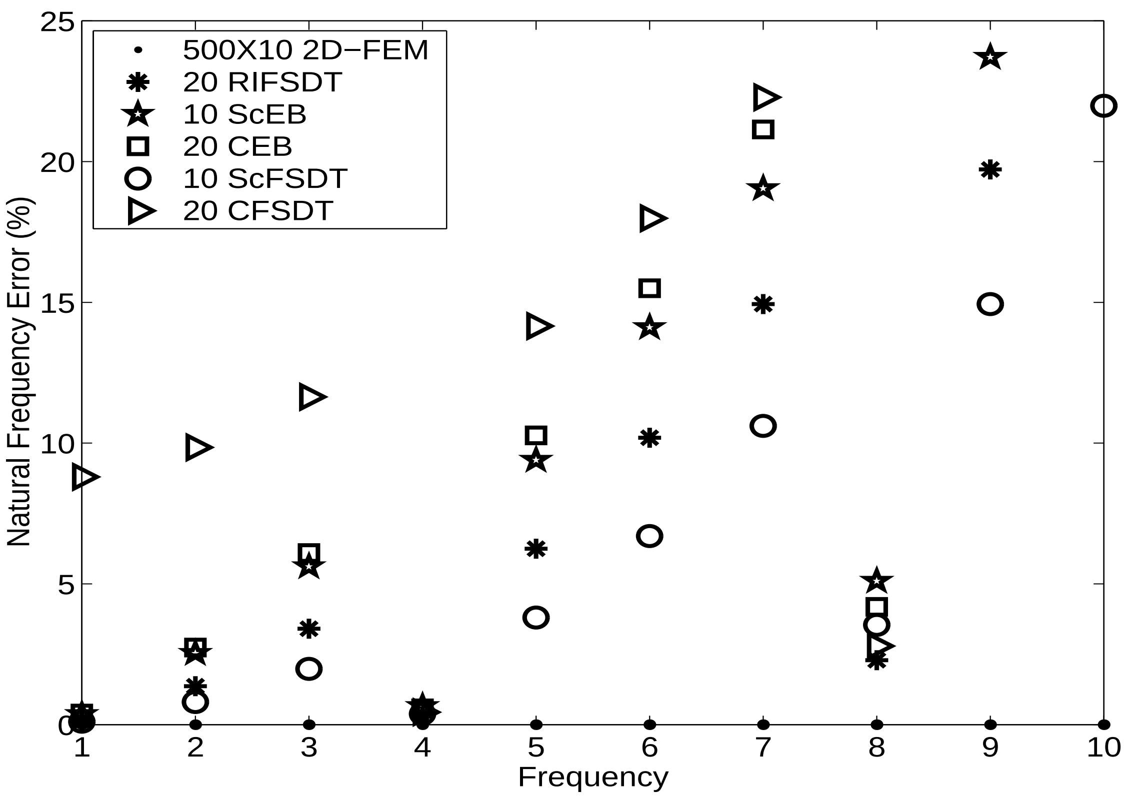

Figure 4.3: Natural Frequency for Cantilever Beam with $[0_5/90_5]$ Layup sequence

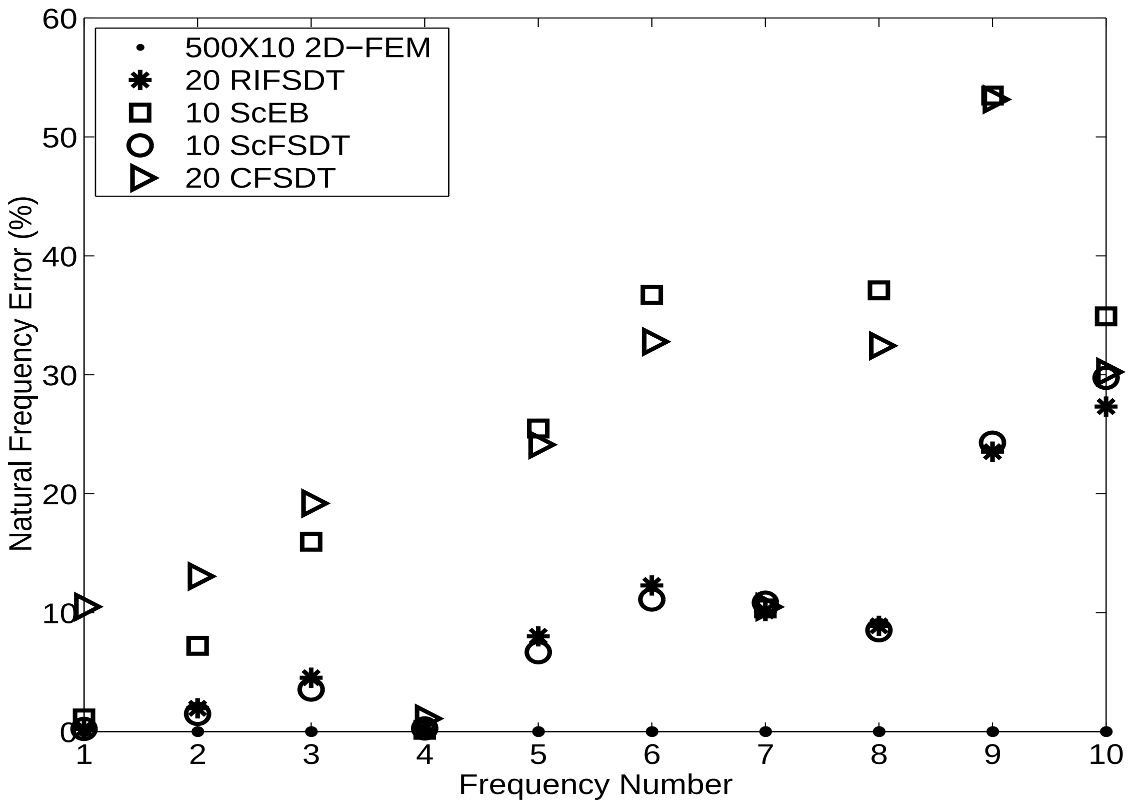

Figure 4.4: Natural Frequency for Beam with Coupled, $[m/0_8/m]$ Layup sequence

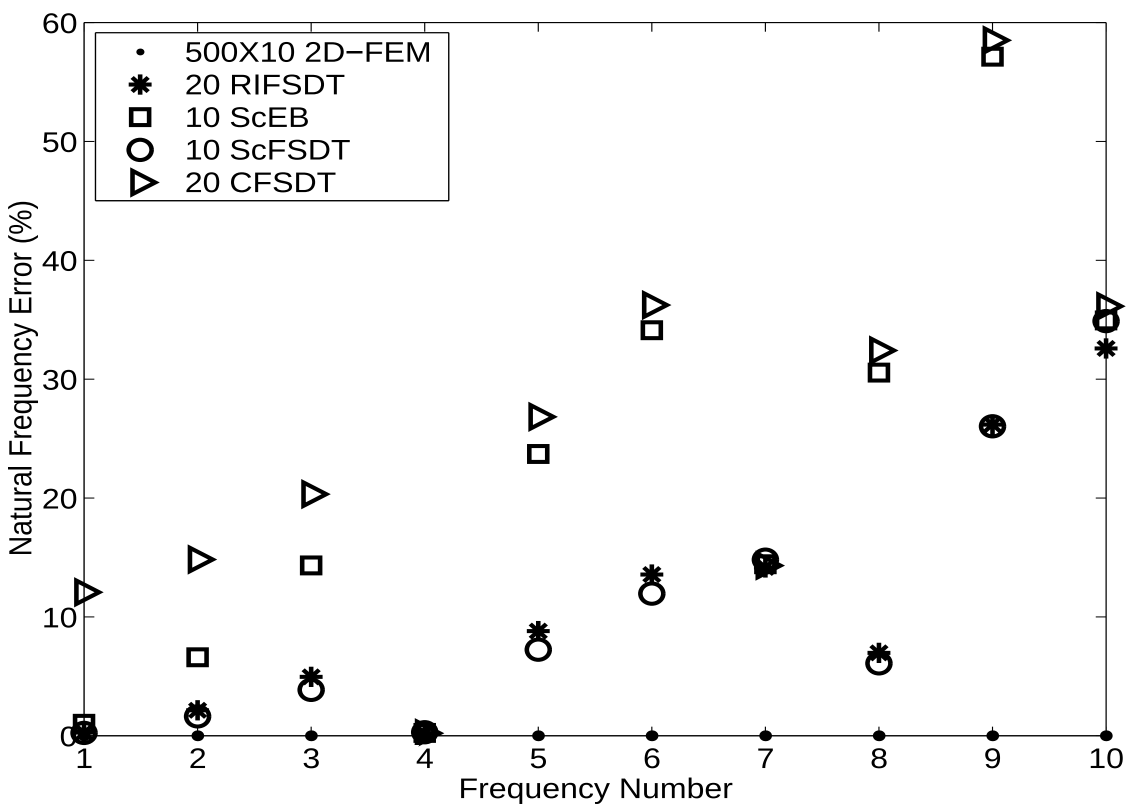

Figure 4.5: Natural Frequency for Beam with Uncoupled, $[m/0_8/m]$ Layup sequence

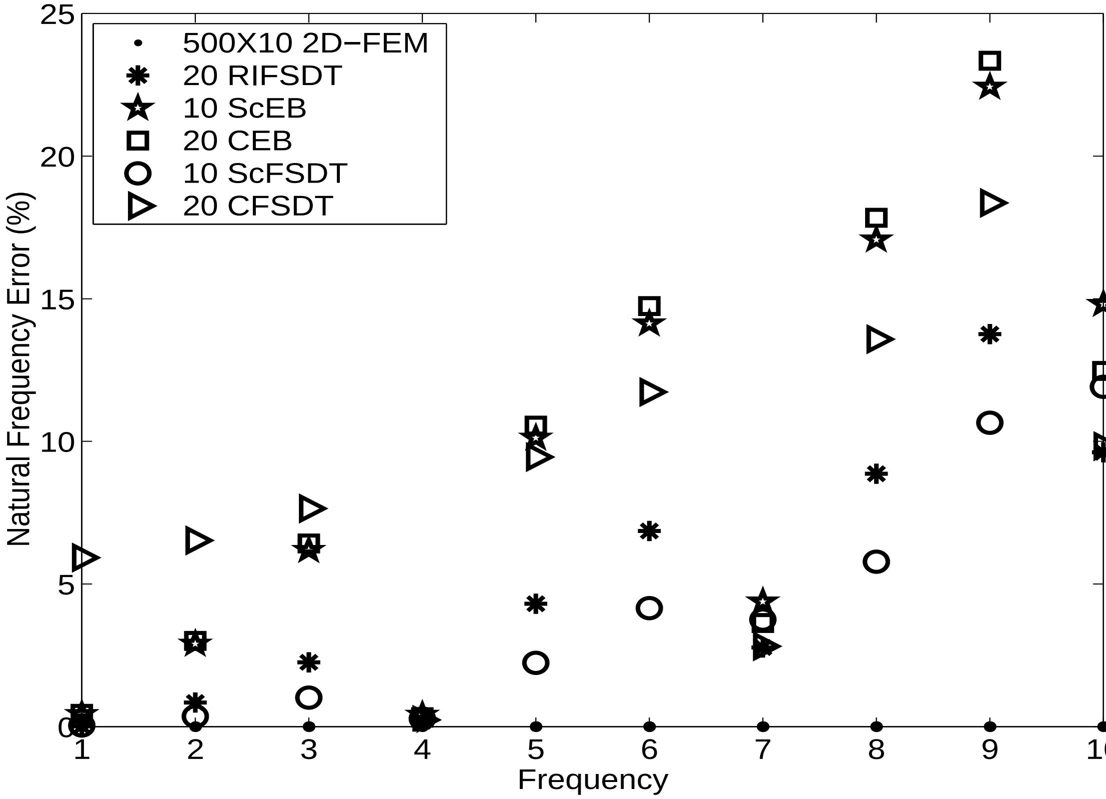

Figure 4.6: Natural Frequency for Beam with Coupled, $[m/0_4/90_4/m]$ Layup sequence

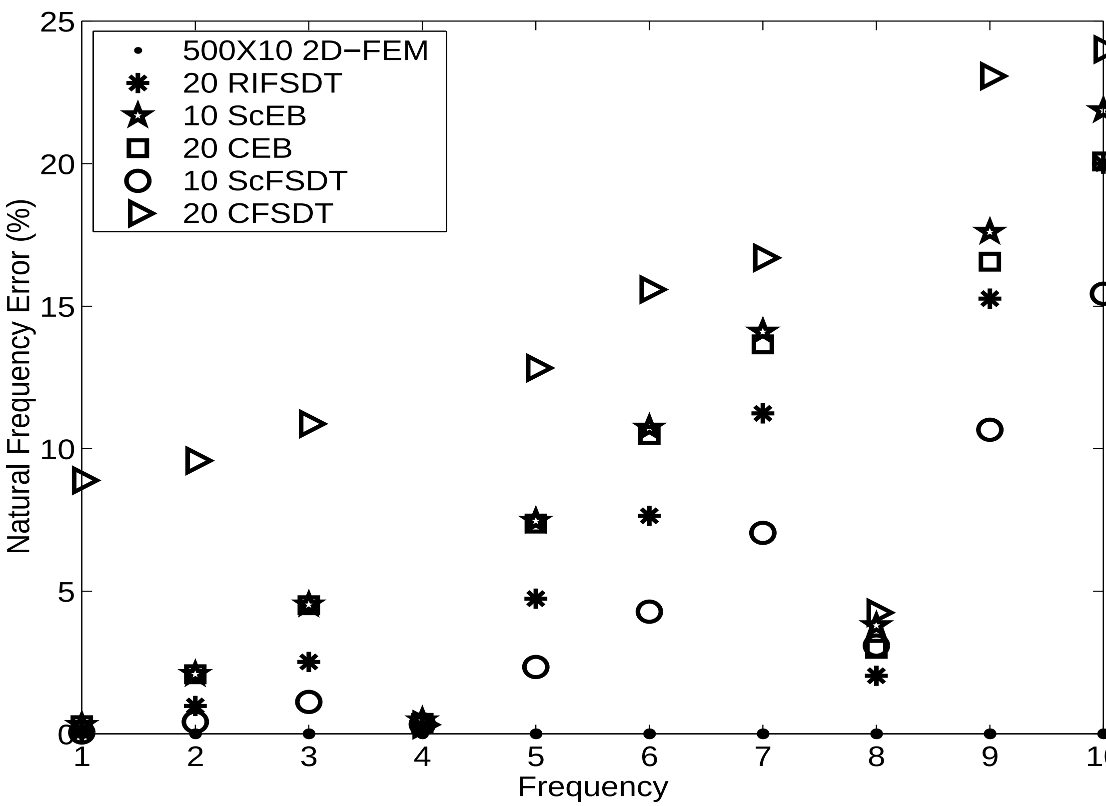

Figure 4.7: Natural Frequency for Beam with Uncoupled, $[m/0_4/90_4/m]$ Layup sequence

Full (CFSDT) gives worst result for this asymmetric layup sequence.

Figure-4.4 and Figure-4.5 show the percentage errors of the first 10 natural frequencies of coupled and uncoupled material model for $[m/0_8/m]$ layup sequence. In this symmetric layup sequence, first 8 natural frequencies with 10 ScFSDT elements give better result than 20 RIFSDT elements. The 9^{th} and 10^{th} natural frequencies for 20 elements RIFSDT give little better result than 10 elements ScFSDT.

Figure-4.6 and Figure-4.7 show the percentage errors of the first 10 natural frequencies of coupled and uncoupled material model for $[m/0_4/90_4/m]$ layup sequence. In coupled formulation, first 9 natural frequencies for 10 ScFSDT elements show better result than 20 RIFSDT elements. Similarly 10 ScEB elements give better result than 20 CEB elements. In uncoupled formulation (where asymmetry is more than in the coupled formulation), for first 10 natural frequencies (except 8^{th}) using 10 ScFSDT elements give better result than 20 RIFSDT elements. Again results from 20 CEB elements are comparable with 10 ScEB elements. Twenty elements of FSDT Full (CFSDT) give worst result for this asymmetric layup sequence. This study to a reasonable extent has shown the superconvergent character of the formulated elements. This can be further studied using the time history analysis, which is given next.

4.3.3.2 Time History Analysis.

Vertical impact load shown in Figure-4.8 is applied at the cantilever tip. Tip response and the open circuit voltage in the sensor coil are obtained for different number of elements for this impact loading. Figure-4.9 shows the effect of beam assumption on tip velocity of the cantilever beam taking 100 elements of ScEB and ScFSDT and the results are compared with 2-D FEM, which is modelled with 1000 2D four noded plane stress element. Two aspects are very clear from this study. A 100 element ScFSDT model compares very well with 2D FEM solution and the waves in shear deformable beams travel much slower compared to elementary beam. This can be seen as early arrival of reflection in ScEB model. Figure-4.10(a) shows the super convergent properties of the ScFSDT element for a unidirectional laminate. Here 10 ScFSDT element model is giving similar result as 20 RIFSDT elements and these match well with 2D FEM solution.

Figure-4.10(b) shows the tip velocity history for $[0_5/90_5]$ layup sequence. Here 10 of ScFSDT elements are giving better result than 20 RIFSDT elements. Figure-4.11 shows the open circuit voltages generated in a laminate of $[m/0_8/m]$ layup sequence due to tip vertical impact. Here 10 ScFSDT elements are giving better result than 20 RIFSDT ele-

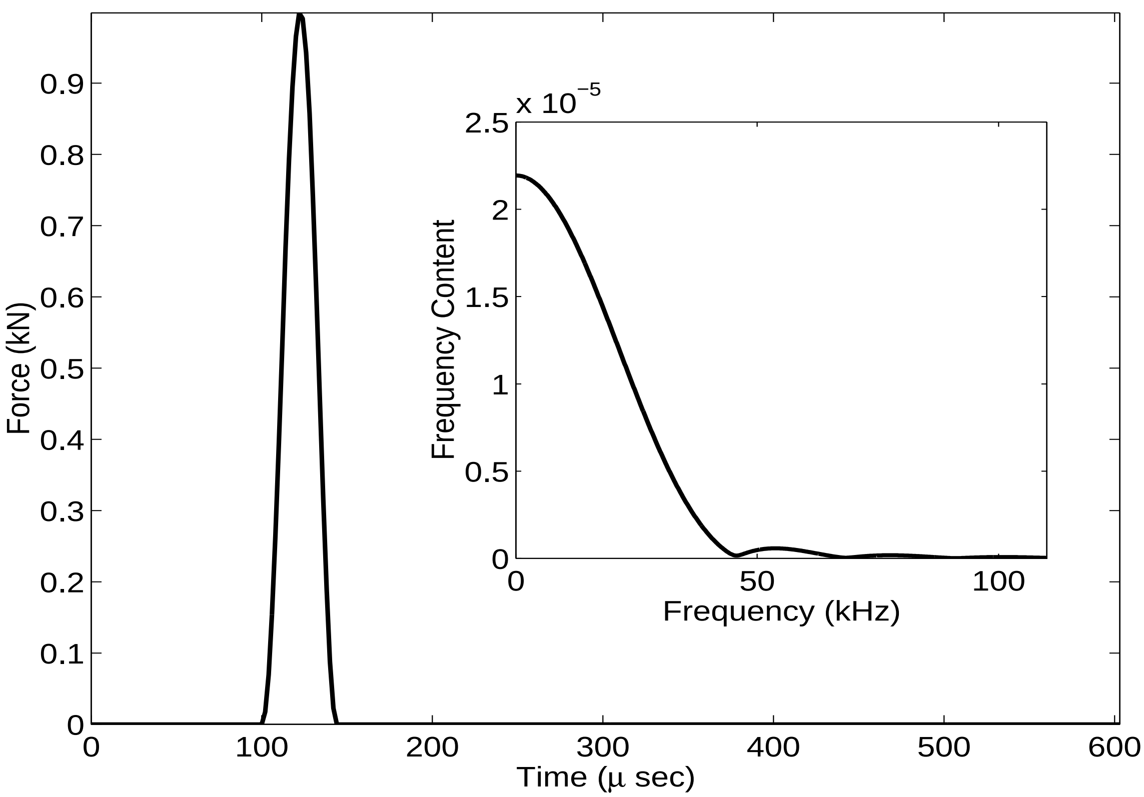

Figure 4.8: 50 kHz Broadband Force History with Frequency Content (inset)

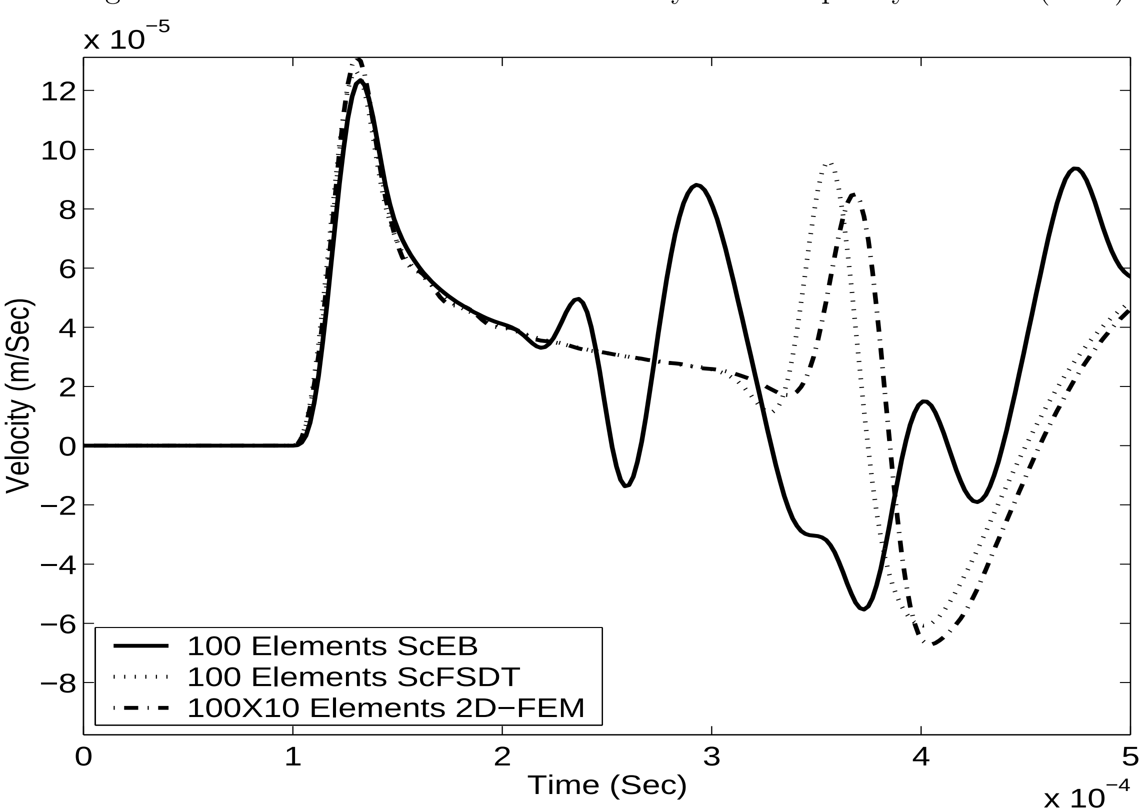

Figure 4.9: Effect of Beam Assumption on Tip Response $[0_{10}]$

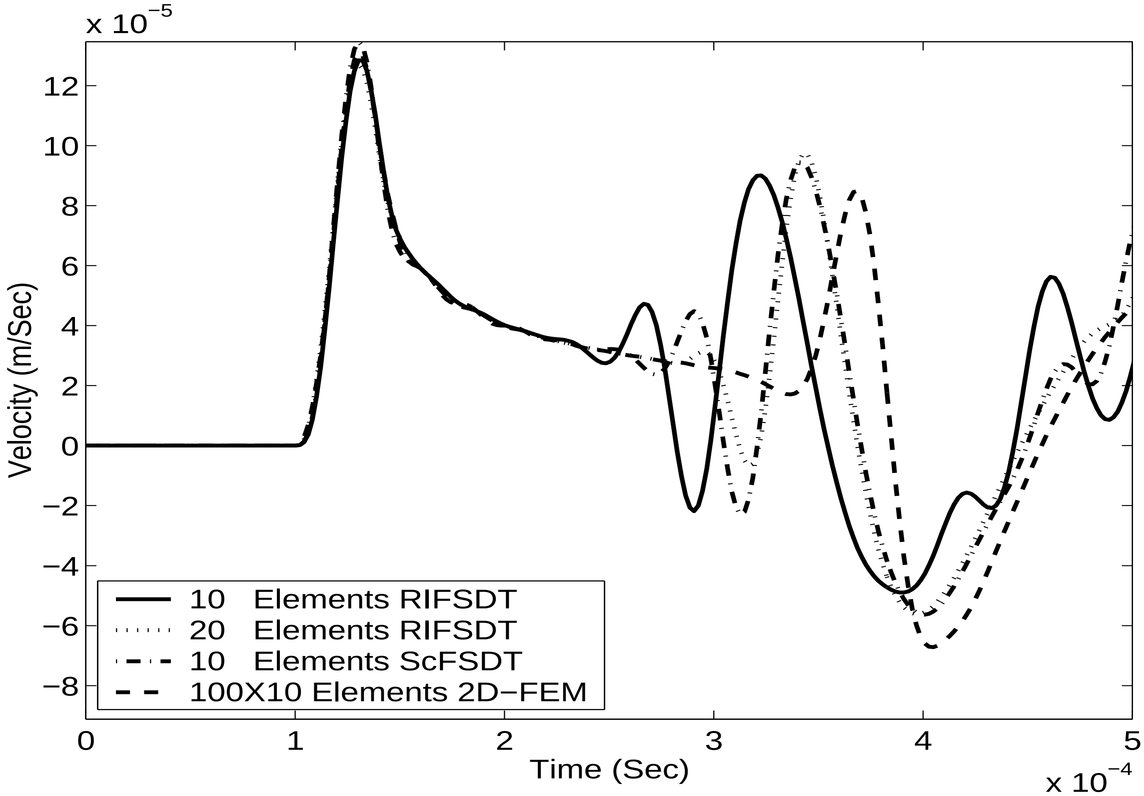

(a) 0_{10} layup sequence

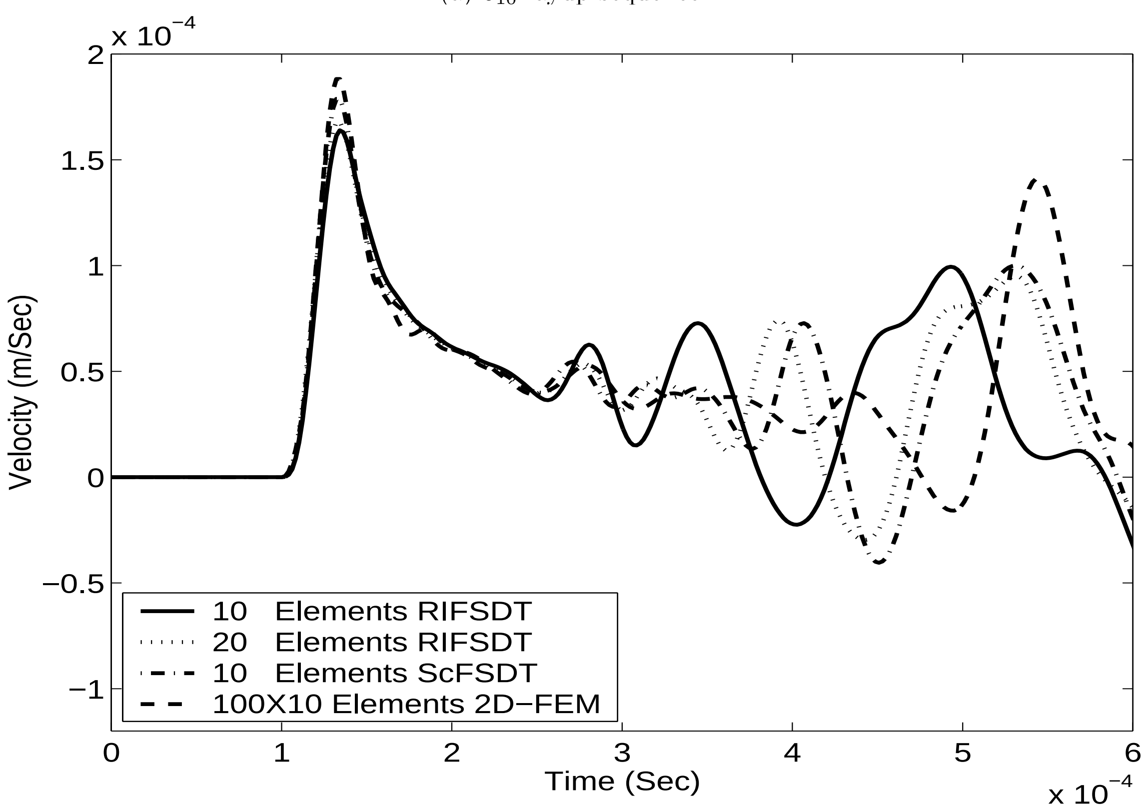

(b) $0_5/90_5$ Layup sequence

Figure 4.10: Superconvergent Study of ScFSDT elements

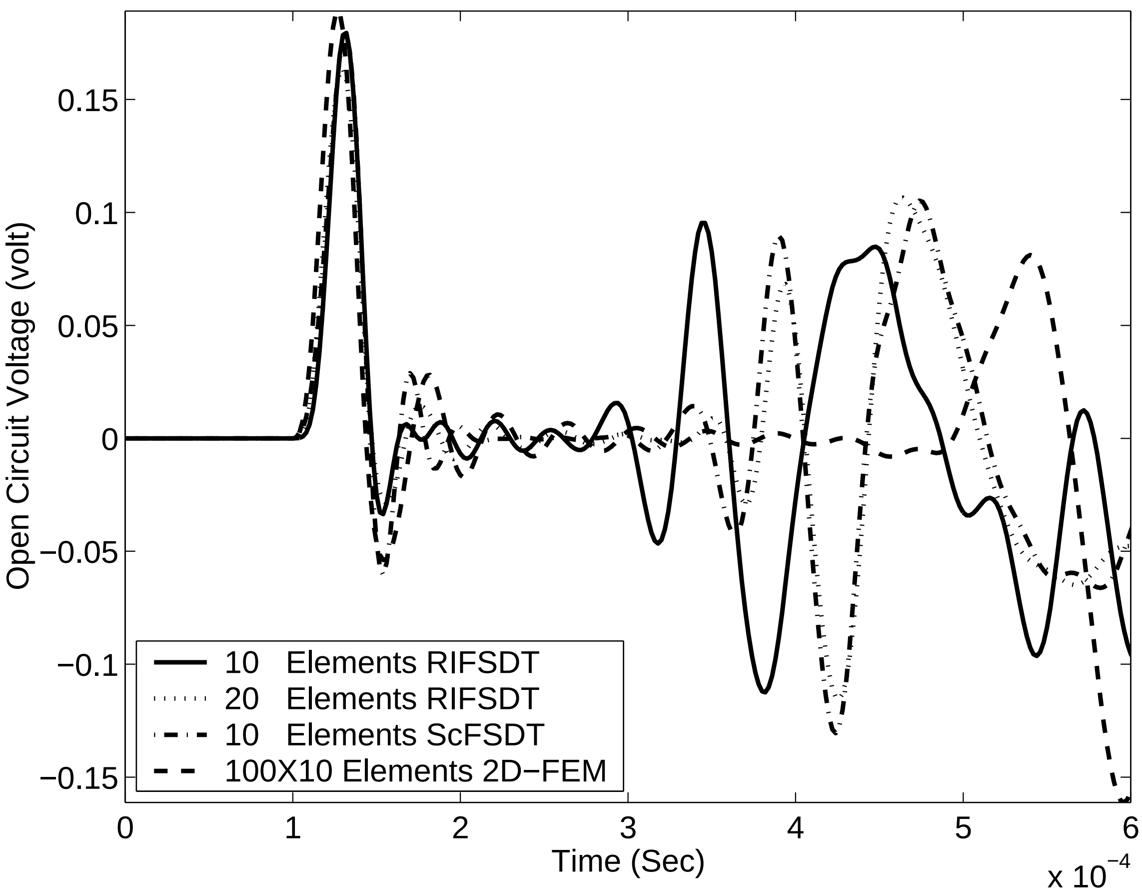

Figure 4.11: Open circuit voltage for Coupled, $[m/0_8/s]$ Layup sequence

ments. These studies have shown that the formulated element is indeed superconvergent and can find great utilities in the SHM application. In the next section, we will use this formulated element to perform an inverse problem of material property identification using the measured response. In this problem, very high degrees of intensive computations are required and the superconvergent property of the formulated element can reduce the problem size considerably.

4.3.4 Material Property Identification

The objective of this subsection is to identify the modulus of elasticity and magnetomechanical coefficient of magnetostrictive patches from the response of sensor using super convergent elements and Artificial Neural Network (ANN). First, the sensor response is computed for varying modulus of elasticity for a particular value of magnetomechanical coefficient and shown that the modulus of elasticity can be identified with a polynomial relationship from peak value of the sensor response. Similarly, in the next study, varying values of magnetomechanical coefficient with fixed value of elastic modulus is used for identification of magnetomechanical coefficient, which also gives a simplified polynomial relationship to identify the magnetomechanical coefficient from peak value of the sensor response. Finally studies are also performed for cases when both the values are varying. Due to the complexity of the problem ANN is used for identification of both elastic modulus and magnetomechanical coefficient.

4.3.4.1 Elastic Modulus Identification

Figure-4.12 shows the sensor response of $[m/0_4/90_4/s]$ layup sequence due to impact load (shown in Figure-4.8) at the tip of the cantilever, where s stands for sensor layer. Considering magnetomechanical coefficient as 15 nano-m/amp and three different values of modulus, three different responses are obtained. Initial peak amplitudes for 25, 30 and 35 GPa module are 323, 468 and 736 mili-volt respectively. The initial peak values (V_p) of these open circuit voltage histories are increased for increased values of modulus of elasticity. One direct polynomial can be used to identify the modulus of elasticity from these peak values or vice versa. From these three sample points, one quadratic polynomial is drawn and elastic modulus (E) or initial peak value (V_p) is expressed as:

$$\begin{aligned} V_p &= 2.462X10^{-3}E^2 - 0.10642E + 1.4447, \\ E &= -38.341{V_p}^2 + 64.822V_p + 8.0588. \end{aligned} \tag{4.61}$$

Now these results are validated for two other values of modulus, namely 27 and 32 GPa, respectively. Initial peak values of voltage histories for corresponding module are 372 and 554 mili-volt respectively from finite element analysis. And the predicted elastic moduli from this polynomial are 26.88 and 32.19 GPa respectively, which are with in 1% of accuracy.

4.3.4.2 Magnetomechanical Coefficient Identification

Figure-4.13 shows the sensor response of the $[m/0_4/90_4/s]$ layup sequence due to impact load (shown in Figure-4.8) at the tip of the cantilever. Considering magnetomechanical coefficient as 5, 10 and 15 nano-m/amp and with a fixed value of modulus as 30 GPa, three different curves are obtained. The initial peak values of open circuit voltages are increased for increased values of magnetomechanical coefficient. One direct polynomial

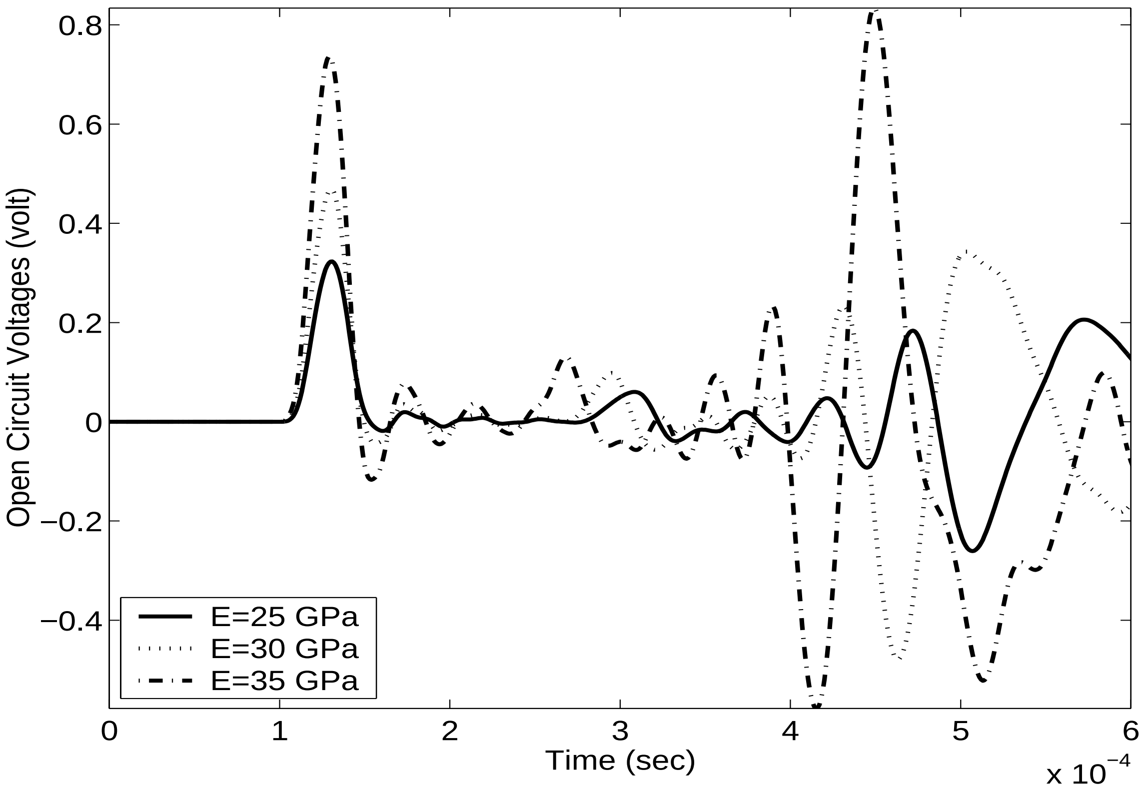

Figure 4.12: Sensor voltage for coupled, $[m/0_4/90_4/s]$ with varying elasticity

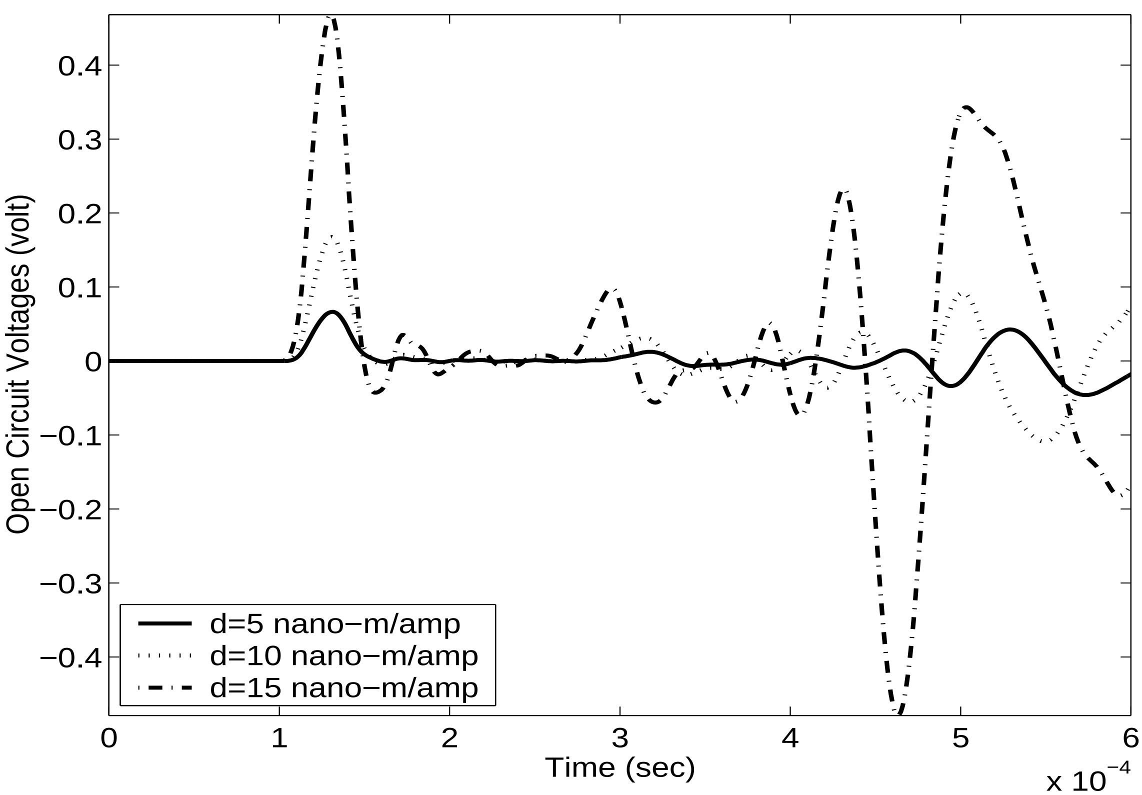

Figure 4.13: Sensor voltage for Coupled, $[m/0_4/90_4/s]$ with varying coupling coefficient

is used to identify the magnetomechanical coefficient from this peak value or vice versa. From these three sample points two quadratic polynomials are drawn as:

$$\begin{aligned} V_p &= 3.9878X10^{15}d^2 - 3.9603X10^7 d + 0.16486, \\ d &= -8.1759X10^{-8}{V_p}^2 + 6.8613X10^{-8}V_p + 7.967. \end{aligned} \tag{4.62}$$

For validation of these curves, two other values of coupling coefficient, namely, 7 and 12 nano-m/amp are used in simulation. Initial peak values considering corresponding coefficients are 99 and 238 mili-volt respectively from finite element analysis. And the predicted coupling coefficients from above polynomial are 6.8 and 12.5 nano-m/amp respectively, which are with in 4% of accuracy.

4.3.4.3 Material Properties Identification using ANN

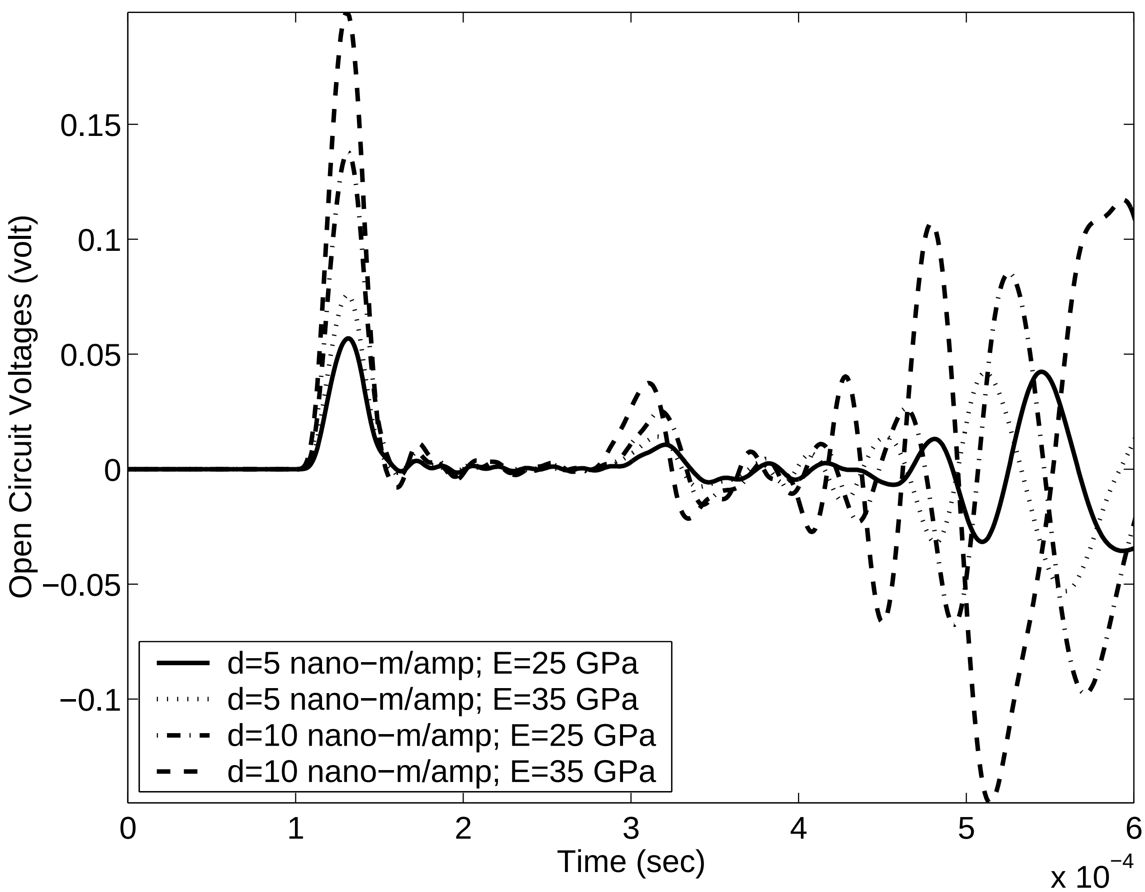

Figure 4.14: Open circuit voltage for Coupled, $[m/0_4/90_4/s]$ layup sequence

In the above discussion, either coupling coefficient is identified assuming elastic modulus of magnetostrictive materials or modulus of elasticity is identified assuming magnetomechanical coupling coefficient. But in real time structural health monitoring application both the values should be identified simultaneously using measured sensor responses. Figure-4.14 shows the sensor response of the $[m/0_4/90_4/s]$ layup sequence due to impact load shown in Figure-4.8 considering both magnetomechanical coefficient and modulus of elasticity as varying. The initial peak value of open circuit voltages are increased due to increase of both these values as shown in earlier two figures. Hence, it is not possible to identify both the properties from initial peak values of open circuit voltages. Hence, utilization of the rest of the response histories is essential in this identification, which can be performed using Artificial Neural Network (ANN) easily.

The main goal of this subsection is to establish a mapping relation from sensor response histories to the material properties. ANN is trained and validated for this mapping. Training of ANN is performed through 121 sample response histories, which are consist of 11 values of elastic modulus (from 25 to 35 GPa with increment of 1 GPa) each for 11 values of magnetomechanical coupling coefficients (from 5 to 15 nano-m/amp with increment of 1 nano-m/amp). Every simulation takes about 30 seconds in Pentium-4 processor with the use of 20 ScFSDT elements. Hence, total time required for simulation of training samples is about one hour. On the other hand, every simulation using 50 RIFSDT elements takes one minute, and hence about 2 hours are required for all samples. Response histories are captured upto 600 time steps. Hence, if raw responses are directly fed into ANN as input, input space of the ANN architecture will be 600, which will be difficult to manage. Hence, some specific peak values and their corresponding location of response histories is considered for input space of the ANN. Whole response histories are divided into three parts. First part is from 0 to 200 μ sec, middle part is from 200 to 400 μ sec, and last part is from 400 to 600 μ sec. In the first part only peak value of response histories (shown in Table-4.6) is taken as first input node for the ANN mapping. Location of the first peak value are not considered as input node of ANN, since the sensitivity of that location regarding elastic modulus or magnetomechanical coefficient is less. From middle and last part of the response histories peak values (shown in Table-4.7, 4.9) and peak locations (shown in Table-4.8, 4.10) are taken as other four input nodes. Total five input nodes are considered as input space of ANN mapping. Two output nodes are considered, one for elastic modulus and other for magnetomechanical coefficient as output space of the ANN mapping. To determine the architecture of the

Table 4.6: First peak amplitude of training samples (mili-volt)

	25	26	27	28	29	30	31	32	33	34	35
5	57	59	61	63	65	67	69	71	73	74	76
6	71	73	75	78	80	83	85	88	90	92	95
7	85	88	91	94	97	100	103	106	109	112	115
8	101	104	108	112	116	120	124	127	131	139	139
9	118	123	128	132	137	142	147	152	156	166	161
10	138	144	150	156	162	168	174	180	187	193	199
11	162	169	177	184	192	199	207	215	224	232	241
12	190	199	208	218	228	238	249	260	271	283	295
13	224	236	248	261	275	289	304	320	337	354	373
14	267	283	300	319	338	360	383	408	435	465	498
15	324	347	373	401	433	469	509	554	605	665	737

Table 4.7: Middle peak amplitude of training samples (mili-volt)

	25	26	27	28	29	30	31	32	33	34	35
5	11	12	12	12	13	13	13	14	14	14	15
6	14	14	15	15	15	16	16	17	17	18	18
7	16	17	17	18	18	19	20	20	21	21	22
8	19	20	20	21	22	22	23	24	25	27	27
9	22	23	24	25	26	27	28	29	30	32	31
10	26	27	28	29	30	32	33	34	35	37	38
11	30	31	33	34	36	37	39	41	42	44	46
12	35	37	39	41	43	45	47	50	52	55	58
13	41	43	46	49	52	55	59	63	67	71	76
14	49	52	56	61	66	71	77	84	92	99	105
15	61	67	73	80	89	99	108	116	120	121	131

Table 4.8: Middle peak location of training samples (micro-second)

	25	26	27	28	29	30	31	32	33	34	35
5	321	320	319	319	318	318	317	317	316	316	316
6	320	320	319	318	318	317	317	316	316	316	315
7	320	319	318	318	317	317	316	316	316	315	315
8	319	318	318	317	317	316	316	315	315	314	314
9	318	318	317	316	316	316	315	314	314	312	313
10	318	317	316	316	315	315	314	313	312	311	311
11	317	316	316	315	314	313	312	311	310	309	308
12	316	315	314	313	312	311	310	308	307	305	303
13	314	313	312	311	309	307	305	304	302	300	298
14	312	310	309	306	304	302	300	298	295	292	289
15	308	306	303	301	298	295	291	287	282	276	268

Table 4.9: Last peak amplitude of training samples (mili-volt)

	25	26	27	28	29	30	31	32	33	34	35
5	43	44	44	44	44	43	42	42	42	42	42
6	52	53	53	52	52	51	50	50	51	52	53
7	61	62	61	60	59	59	59	60	61	63	64
8	70	70	69	68	67	68	69	71	73	76	76
9	79	77	77	77	78	80	82	84	86	89	87
10	86	86	87	89	91	93	95	96	99	102	108
11	95	97	99	101	103	105	108	114	123	132	141
12	108	110	111	113	118	127	139	151	160	166	171
13	119	120	127	141	156	169	178	184	189	195	201
14	136	153	171	185	194	200	208	217	220	214	202
15	184	199	207	218	230	233	223	209	216	234	234

Table 4.10: Last peak location of training samples (micro-second)

	25	26	27	28	29	30	31	32	33	34	35
5	545	542	539	535	532	529	526	522	518	515	511
6	543	539	536	533	529	526	521	517	514	511	507
7	540	536	533	529	525	520	516	512	509	507	502
8	536	532	528	524	519	514	511	507	503	498	498
9	532	527	522	517	512	508	504	500	498	489	493
10	526	520	515	511	505	502	498	493	488	484	479
11	518	512	507	502	498	493	487	482	477	472	468
12	511	504	499	493	486	480	475	470	465	460	456
13	500	493	486	479	473	467	462	456	450	444	439
14	487	479	472	465	459	452	444	438	431	425	417
15	472	464	456	447	439	431	423	414	404	396	389

ANN, four different ANN (5-2-2;5-3-2;5-4-2;5-5-2) are considered with the above mentioned training samples. Training histories of these networks are shown in Figure-4.15. Figure shows, ANN architecture (5-4-2) with four hidden layer nodes (Figure-4.16(c)) gives better training performance, and this architecture is considered for the subsequent studies. Figure-4.16(c) shows the ANN architecture with 5 input nodes, 2 output nodes and one hidden layer with 4 hidden nodes. Two output nodes are for modulus of elasticity and coupling coefficient, where as input nodes, which are five in number corresponding to the five values obtained from response histories as discussed earlier. After the training of the ANN using training samples, these same samples are simulated in the trained ANN to check the training performance of the ANN. Figure-4.17 shows the training performance of this ANN after 10000 epoch of training. Expected and predicted location in the output

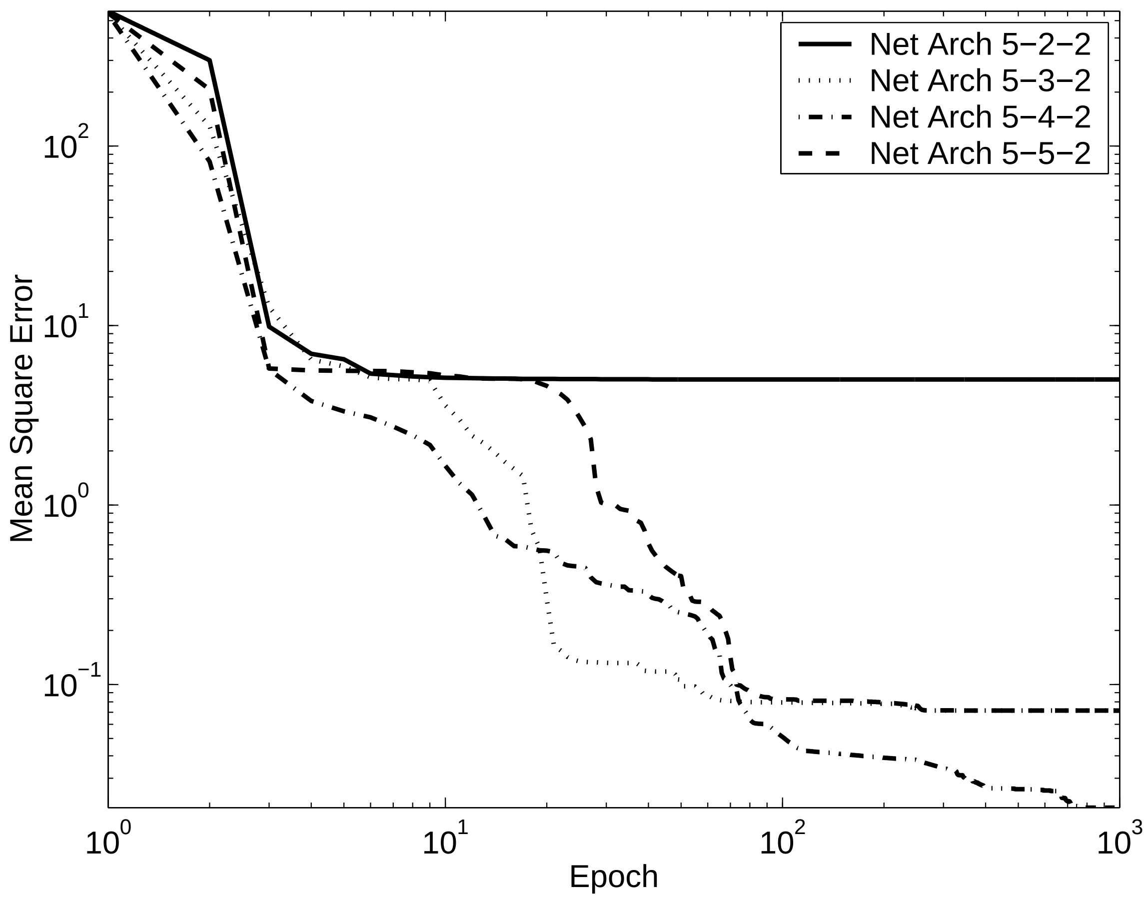

Figure 4.15: Training Histories of different ANN architectures

space of the training samples are shown as $'*'$ and $'\circ'$ respectively. After checking the training performance for generalization of the mapping, networks are validated with a different set of samples, which are not been used for training purpose in the network. For validation, 100 intermediate sample response histories are obtained in finite element simulation, which are for 10 values of elastic modulus (from 25.5 to 34.5 GPa with increment of 1 GPa) each for 10 values of magnetomechanical coupling coefficients (from 5.5 to 14.5 nano-m/amp with increment of 1 nano-m/amp). Similar to training phase, five input nodes of ANN mapping are extracted from these response histories and given in Tables-4.11, 4.12, 4.13, 4.14, and 4.15, respectively. Finally, these validation samples are used to simulate in ANN and corresponding prediction for both elastic modulus and magnetomechanical coupling coefficient are obtained. Figure-4.18 shows the validation performance of the network, where expected and predicted location in the output space

Table 4.11: First peak amplitude of validation samples (mili-volt)

	25.5	26.5	27.5	28.5	29.5	30.5	31.5	32.5	33.5	34.5
5.5	64	66	68	71	73	75	77	79	81	83
6.5	78	81	83	86	89	92	94	97	100	102
7.5	93	97	100	104	107	110	114	117	120	124
8.5	110	115	119	123	127	132	136	140	144	149
9.5	130	135	140	145	151	156	162	167	173	178
10.5	152	158	165	172	179	185	192	199	207	214
11.5	178	186	195	204	212	221	230	240	250	260
12.5	210	221	232	243	255	267	280	293	307	322
13.5	250	264	279	295	311	329	348	368	390	414
14.5	301	321	343	367	392	421	452	487	526	569

Table 4.12: Middle peak amplitude of validation samples (mili-volt)

	25.5	26.5	27.5	28.5	29.5	30.5	31.5	32.5	33.5	34.5
5.5	12	12	12	13	13	14	14	14	15	15
6.5	14	15	15	16	16	17	17	18	18	19
7.5	17	18	18	19	19	20	21	21	22	23
8.5	20	21	21	22	23	24	25	26	27	27
9.5	23	24	25	26	27	28	30	31	32	33
10.5	27	28	30	31	33	34	35	37	38	40
11.5	32	33	35	37	39	41	43	45	47	49
12.5	38	40	42	44	47	50	53	56	60	63
13.5	45	48	51	55	59	64	68	73	79	86
14.5	55	60	66	72	78	86	95	103	110	115

Table 4.13: Middle peak location of validation samples (micro-second)

	25.5	26.5	27.5	28.5	29.5	30.5	31.5	32.5	33.5	34.5
5.5	320	320	319	318	318	317	317	316	316	316
6.5	320	319	318	318	317	317	316	316	316	315
7.5	319	319	318	317	317	316	316	316	315	315
8.5	319	318	317	317	316	316	315	315	314	313
9.5	318	317	317	316	316	315	314	313	313	312
10.5	317	316	316	315	314	313	312	312	311	310
11.5	316	315	314	313	312	311	310	309	308	307
12.5	315	313	312	311	310	309	307	305	303	302
13.5	312	311	310	308	306	304	302	300	298	296
14.5	310	307	305	302	300	298	295	292	288	284

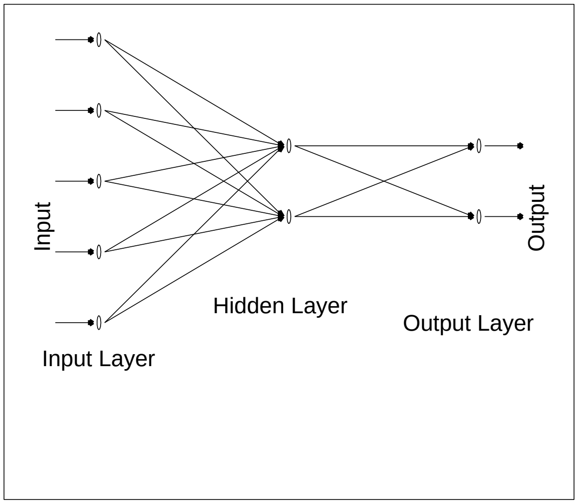

(a) 5-2-2 architectures

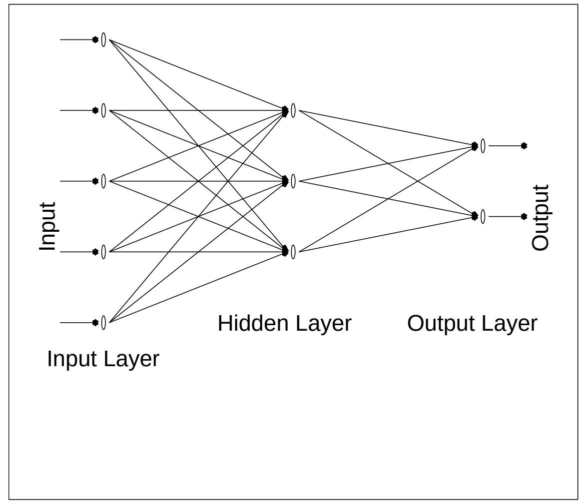

(b) 5-3-2 architectures

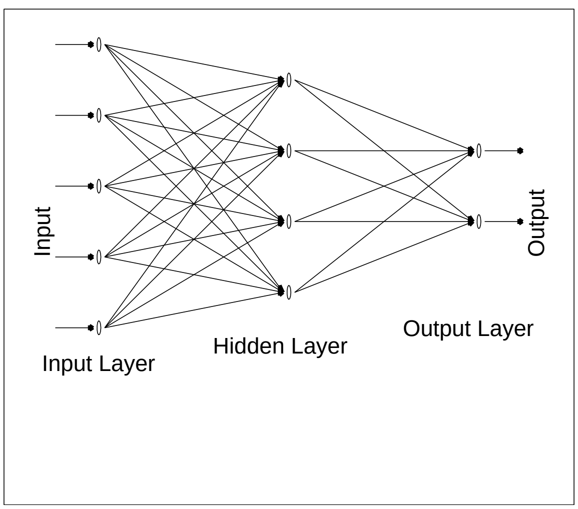

(c) 5-4-2 architectures

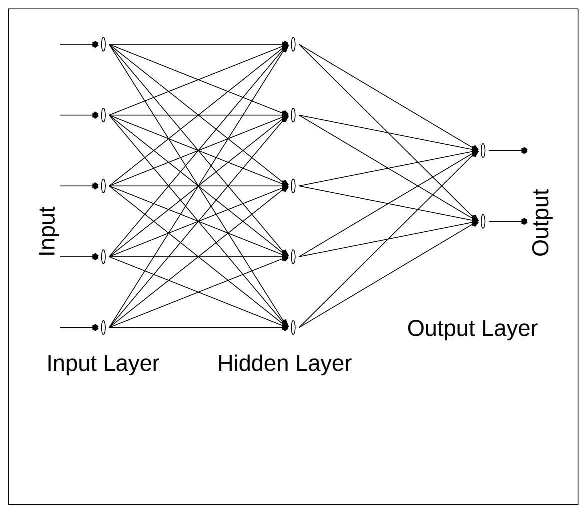

(d) 5-5-2 architectures

Figure 4.16: ANN with Different architectures

of the validation samples are shown as $'\square'$ and 'x' respectively. Using these ANN, feeding any response histories, the corresponding elastic modulus and magnetomechanical coupling coefficient can be identified with in 1% accuracy.

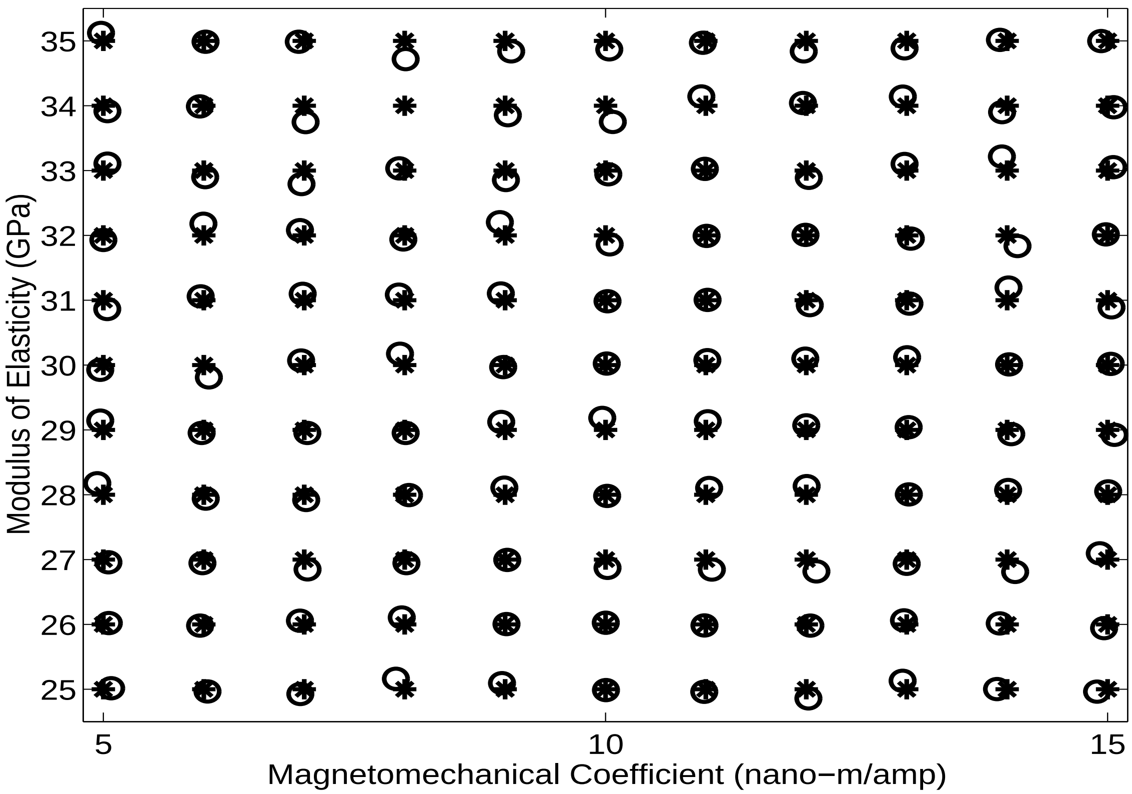

Figure 4.17: Training Performance of 5-4-2 ANN architectures

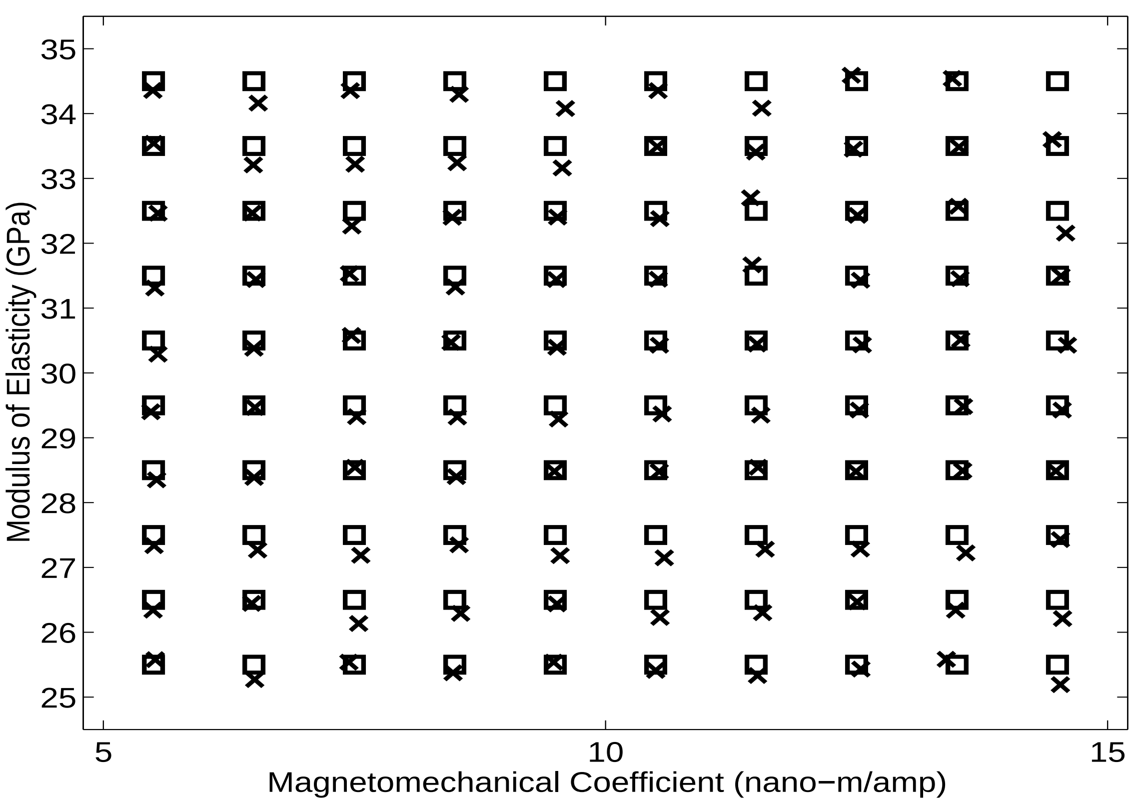

Figure 4.18: Validation Performance of 5-4-2 ANN architectures

Table 4.14: Last peak amplitude of validation samples (mili-volt)

	25.5	26.5	27.5	28.5	29.5	30.5	31.5	32.5	33.5	34.5
5.5	47	47	48	47	46	46	45	45	45	46
6.5	56	56	56	55	54	53	53	54	55	57
7.5	65	65	64	62	62	62	64	65	67	68
8.5	73	72	71	71	72	74	76	78	79	81
9.5	81	80	81	82	84	86	88	90	92	94
10.5	90	91	93	95	97	98	101	104	110	118
11.5	102	104	105	107	110	115	124	135	145	153
12.5	113	114	118	127	140	153	164	171	176	180
13.5	126	137	154	170	181	188	193	201	208	212
14.5	167	184	195	203	213	223	226	217	203	508

Table 4.15: Last peak location of validation samples (micro-second)

	25.5	26.5	27.5	28.5	29.5	30.5	31.5	32.5	33.5	34.5
5.5	542	539	536	533	529	526	522	518	514	510
6.5	540	536	533	529	525	521	517	513	510	506
7.5	536	533	529	524	520	515	510	508	505	501
8.5	532	528	523	518	514	509	506	501	499	495
9.5	526	521	516	510	506	503	499	495	491	487
10.5	519	514	509	504	500	495	490	485	480	476
11.5	510	506	501	495	490	484	478	473	469	465
12.5	501	496	490	483	477	471	466	461	456	450
13.5	490	483	476	469	463	457	451	444	438	432
14.5	476	469	461	454	446	438	431	424	415	468

4.4 Summary

This study is mainly intended to explore the use of superconvergent FE formulation for the analysis of smart composite structures with magnetostrictive patches and their utility in solving inverse problems. Classical and shear deformable beam elements for the analysis of composite beam with embedded magnetostrictive patches are formulated. The consistent mass matrix is derived using the exact solution to the static part of governing equation. Rotary inertia is also taken into account. The formulated element is then used to study the superconvergent property in static, free vibration, and wave propagation problems in composite beams embedded with magnetostrictive patches. The effect of superconvergence was shown in all these problems. The formulated element was later used for identification of the magnetostrictive material properties using using artificial neural network, where superconvergent elements are utilized to get sensor response in finite element simulation with lesser computation time, where ANN is used for mapping from sensor response to properties of the magnetostrictive materials. In the next chapter, we will again concentrate on developing better and more accurate numerical / analytical model for analysis of smart laminated composite structure. This model is called the spectral finite element model.